

Analysis and optimization of NDVI definitions and areal fraction models in remote sensing of vegetation

X. ZHOU*†, H. GUAN‡**, H. XIE§ and J. L. WILSON‡

†Department of Geophysical Engineering, Montana Tech of the University of Montana, Butte, MT 59701, USA

‡Department of Earth and Environmental Science, New Mexico Tech, Socorro, NM 87801, USA

§Laboratory for Remote Sensing and Geoinformatics, University of Texas at San Antonio, San Antonio, TX 78249, USA

(Received 26 December 2006; in final form 24 July 2008)

Variations in the definition of the Normalized Difference Vegetation Index (NDVI) and inconsistencies in vegetation areal fraction models prejudice the understanding of long-term variability and change in land cover. We analysed the consequences of using NDVI definitions based on the digital number (DN), spectral radiance and spectral reflectance for six active and high spatial resolution multi- and hyperspectral satellite sensors (ALI, ASTER, ETM+, HRVIR, Hyperion and IKONOS) and optimized the NDVI definitions, and then examined the performance of three vegetation areal fraction models: the linear reflectance, linear NDVI and quadratic NDVI models. The examination was performed for three plots chosen from two biomass zones: a short and small leaf area index (LAI) creosote shrub zone, and a tall and large-LAI piñon-juniper zone. The results show that: (1) the difference in NDVI values among the NDVI definitions is sensor dependent and always significant; spectral reflectance should be used in NDVI calculations, and using radiance or DN values in calculating the NDVI should be avoided; (2) in deriving vegetation areal coverage, the linear reflectance model outperforms the other two models in the shrub biomass zone; and (3) the linear NDVI model outperforms the other two models in the piñon-juniper biomass zone. These observations are consistent with the fact that the non-linear effect is less important in shrubland than in piñon-juniper woodland and that the linear NDVI model is more capable of capturing non-linearity in the spectral analysis.

1. Introduction

Vegetation areal coverage is an important parameter in the understanding of long-term variability and change in land cover. Monitoring regional (or global) vegetation greenness and coverage is often based on spectral reflectance and the widely used Normalized Difference Vegetation Index (NDVI), which provides a measure indicating the vigour of vegetation (e.g. Campbell 1987, Bannari *et al.* 1995, Xie *et al.* 2007), an ecological surrogate measure of the absorbed photosynthetically

*Corresponding author. Email: XZhou@mtech.edu

**Present address: School of Chemistry, Physics and Earth Sciences, Flinders University, Australia.

active radiation (APAR) and thus photosynthetic activity in the vegetation (e.g. Asrar *et al.* 1984, Daughtry *et al.* 1992, Myneni *et al.* 1995), and also the leaf area index (LAI), which is one of the key inputs in models describing biosphere processes (Nemani *et al.* 1993, Running *et al.* 1999, Chen *et al.* 2004, Kalácska *et al.* 2004, Shabanov *et al.* 2005, Soudani *et al.* 2006).

Unfortunately, the definition of the NDVI derived from remotely sensed optical data in the literature is often not unique (Steven *et al.* 2003). The NDVI was first proposed for studying the vernal advancement and retrogradation of vegetation by Rouse *et al.* (1973). It was then used to monitor vegetation and detect changes in regional and global vegetation canopy (Tucker 1979, Justice *et al.* 1985, Tucker *et al.* 1985a, Cihlar *et al.* 1991). In Rouse's initial definition, the NDVI is calculated using spectral reflectance. However, the first vegetation indices were developed using raw satellite digital numbers (DNs) or digital counts, without transformation into radiance and reflectance, atmospheric corrections, and sensor calibration (Bannari *et al.* 1995). Later researchers also used other spectral quantities in the calculation of the NDVI. Most publications in the remote sensing literature followed Rouse's initial definition and the NDVI was computed from spectral reflectances of the near-infrared (R_{nir}) and the red (R_r) reflected bands from the surface and transmitted through the atmosphere (Rouse *et al.* 1973, Myneni *et al.* 1995). Using spectral reflectance to calculate the NDVI, Guyot and Gu (1994) clarified that a radiometric correction has to be performed. There are also several publications that used spectral radiance in the calculation of the NDVI (e.g. Oguro *et al.* 2001, Hunt *et al.* 2002, Johnson *et al.* 2003, Lu *et al.* 2003, Ingram *et al.* 2005). Some used DN values directly (e.g. Chrysoulakis 2003, Colombo *et al.* 2003). Others mentioned that 'spectral data' were used but did not specify whether they used spectral reflectance or spectral radiance data or DN values (e.g. Paruelo and Lauenroth 1995). Realizing the various definitions of the NDVI using the DN value, spectral radiance and spectral reflectance, some authors used some or all of these definitions in studies of multisensor intercomparisons or relationships between vegetation characteristics and vegetation indices (Vierling *et al.* 1997, Turner *et al.* 1999, Gupta *et al.* 2001, Thenkabail *et al.* 2004, Soudani *et al.* 2006).

Since the NDVI is easier to obtain from remotely sensed data than the vegetation areal fraction itself, numerous studies have been carried out to establish a relationship between vegetation areal fraction and the NDVI or spectral reflectance, resulting in various empirical or semiempirical models. These include the linear NDVI model (e.g. Wittich and Hansing 1995, Gutman and Ignatov 1998, Leprieur *et al.* 2000, Qi *et al.* 2000, Zeng *et al.* 2000, Lu *et al.* 2003), the quadratic NDVI model (e.g. Choudhury *et al.* 1994, Carlson and Ripley 1997, Gillies *et al.* 1997) and the linear reflectance model (e.g. Smith *et al.* 1990a,b, Roberts *et al.* 1993, 1998, Asner and Heidebrecht 2002). Considering the multiplicity of NDVI definitions, NDVI-based vegetation areal fraction models (the linear NDVI model and the quadratic NDVI model) are not uniquely defined.

To reduce the ambiguity in applying the NDVI-based vegetation areal fraction models, the various definitions of NDVI need to be analysed and optimized so that other convolving factors can be unfolded. For instance, as these models were derived either from simplified physical models or from empirical models based on data collected under specific conditions, use of these models generally results in inconsistencies in estimating areal coverage of vegetation. Is this inconsistency due to the multiple definitions of NDVI? By intercomparison of the NDVI values using

different quantities (DN values, spectral radiance, and spectral reflectance), we have investigated whether the multiple definitions are consistent with each other and with the ground truth. Based on the assessment of the multiple definitions of NDVI, we optimized the NDVI definitions; and based on the optimized NDVI definition, NDVI-based vegetation areal fraction models were thus defined. Then we identified which of the vegetation areal fraction models was most consistent with the ground measurements.

Analysis and optimization of NDVI definitions and vegetation areal fraction models have to be carried out using remotely sensed data from specific sensors. In this study, we only focused on the sensors that are currently in operation and have high spatial resolution (<100 m). These (table 1) include the Advanced Land Imager (ALI) (NASA 2002, USGS 2006), the Advanced Spaceborne Thermal Emission and Reflection Radiometer (ASTER) (Abrams *et al.* 2002), the Enhanced Thematic Mapper Plus (ETM+) onboard Landsat-7 (NASA 2006), Hyperion (USGS 2006), IKONOS (Dial *et al.* 2003), and the High-Resolution Visible and Infrared (HRVIR) detector onboard SPOT (Schroeder *et al.* 2001). ASTER consists of three different subsystems but only the three bands of the visible and near-infrared (VNIR) subsystem with a spatial resolution of 15 m were included. The high spatial resolution data from these sensors are often used for virtual ground truthing by validating conclusions derived from the coarser spatial resolution systems (Morisette *et al.* 2003) and to monitor changes in land use and land cover (Coca *et al.* 2004).

2. Variety of NDVI definitions and the consequences

If we accept the three definitions of the NDVI using the DN value, spectral radiance and spectral reflectance, then the NDVI at each pixel is calculated by the following equations:

$$\text{NDVI}_{\text{DN}} = \frac{(\text{DN}_{\text{nir}}) - (\text{DN}_{\text{r}})}{(\text{DN}_{\text{nir}}) + (\text{DN}_{\text{r}})} \quad (1)$$

$$\text{NDVI}_{\text{L}} = \frac{L_{\text{nir}} - L_{\text{r}}}{L_{\text{nir}} + L_{\text{r}}} \quad (2)$$

$$\text{NDVI}_{\text{R}} = \frac{R_{\text{nir}} - R_{\text{r}}}{R_{\text{nir}} + R_{\text{r}}} \quad (3)$$

where DN, L and R denote the DN value, spectral radiance and spectral reflectance, respectively. NDVI_{DN} , NDVI_{L} and NDVI_{R} are the NDVI defined using the DN value, spectral radiance and spectral reflectance, respectively. The subscript nir denotes the near-infrared band and r denotes the red band. The NDVI varies within a bounded range from -1 to 1 but is defined as zero when the values of DN, spectral radiance or spectral reflectance of the nir and red bands are zero. As the reflected signal of vegetation usually decreases in the red band due to absorption of solar energy by chlorophyll and increases in the near-infrared due to strong back-scattering by the spongy parenchyma's cell structure (Tucker *et al.* 1985b, Buschmann and Nagel 1993), the NDVI is sensitive to the presence of vegetation and is thus used to indicate vernal advancement and retrogradation of vegetation.

The general procedure to obtain spectral reflectance from the DN or digital counts consists of two steps. First, the DN value is converted to spectral radiance

Table 1. Sensors studied and lookup table for conversion from DN values to spectral radiance. Subscript i denotes the i th pixel and subscript j denotes the j th band. CC_j is a coefficient of the j th band in equations (T3) and (T6). In equation (T8), CD_j is a coefficient and BW_j is the bandwidth corresponding to the j th band.

Sensor	DN to radiance L_{ij} ($W m^{-2} sr^{-1} \mu m^{-1}$)	DN _{ij}	Notes			
ALI	T1: $L_{ij} = DN_{ij}/30$ (before 22 December 2004)	16-bit	Band j (μm)	S_j	OS_j	
			1p (0.433–0.453)	0.45	–34	
			1 (0.450–0.515)	0.43	–44	
			2 (0.425–0.605)	0.28	–19	
			3 (0.633–0.690)	0.18	–13	
	T2: $L_{ij} = DN_{ij} \cdot S_j + OS_j$ (on or after 22 December 2004)	16-bit	4 (0.775–0.805)	0.11	–8.5	
			4p (0.845–0.890)	0.091	–6.5	
			5p (1.200–1.300)	0.083	–13	
			5 (1.550–1.750)	0.028	–6	
			7 (2.080–2.350)	0.0091	–2.1	
ASTER	T3: $L_{ij} = (DN_{ij} - 1)/CC_j$	8-bit	Band (μm)	CC_j ($W^{-1} m^2 sr \mu m$)		
				HG mode	NG mode	LG mode
			1 (0.52–0.60)	0.676	1.688	2.25
			2 (0.63–0.69)	0.708	1.415	1.89
			3* (0.78–0.86)	0.423	0.862	1.15
ETM+	T4:	8-bit	T4: for LPGS products			
	$L_{ij} = \frac{L_{max,j} - L_{min,j}}{254} (DN_{ij} - 1) + L_{min,j}$					
	T5:		T5: for NLAPS products			
	$L_{ij} = \frac{L_{max,j} - L_{min,j}}{255} DN_{ij} + L_{min,j}$		$L_{max,j}$ and $L_{min,j}$ should be found in the image header file			

Table 1. (Continued.)

Sensor	DN to radiance L_{ij} ($\text{W m}^{-2} \text{sr}^{-1} \mu\text{m}^{-1}$)	DN_{ij}	Notes	
HRVIR	T6: $L_{ij} = \text{DN}_{ij} / \text{CC}_j$	8-bit	Band (μm)	
			CC_j ($\text{W}^{-1} \text{m}^2 \text{sr} \mu\text{m}$)	
			1 (0.500–0.590)	1.55678
			2 (0.61–0.68)	1.89702
			3 (0.78–0.89)	1.27415
4 (1.58–1.75)	9.018			
Hyperion	T7: $L_{ij} = \text{DN}_{ij} / 40$ (for VNIR)	16-bit	For Hyperion, bands 33 (0.6812 μm) and 45 (0.8033 μm) are used for NDVI calculation (Pearlman 2003, Asner <i>et al.</i> 2004)	
IKONOS	T8: $L_{ij} = \text{DN}_{ij} / \text{CD}_j / \text{BW}_j$	11-bit	Band (μm)	
			CD_j ($\text{W}^{-1} \text{m}^2 \text{sr}$)	
			(before 22 February 2001) (after 22 February 2001)	
			BW_j (μm)	
			1 (0.445–0.516)	63.3
2 (0.506–0.595)	64.9	72.7	0.0886	
3 (0.632–0.698)	84.0	94.9	0.0658	
4 (0.757–0.853)	74.6	84.3	0.0954	

S, scale factor; OS, offset; HG, high gain; NG, normal gain; LG, low gain modes.

* The two bands (3B, backward looking and 3N, nadir looking) of ASTER band 3 have the same characteristics.

using information on gain and offset. This step is the reverse of digitizing the analogue signal, representing radiance through instrument calibration. Therefore, the relationship between the DN value and the spectral radiance is generally given at the stage of product generation. Table 1 shows these relationships, where L_{ij} is the spectral radiance (in $\text{W m}^{-2} \text{sr}^{-1} \mu\text{m}^{-1}$) at the i th pixel for the j th band and BW_j is the band width in units of μm of the j th band. The second step is the conversion of spectral radiance to spectral reflectance. This is accomplished by using the following formula (NASA 2006):

$$R_j = \frac{\pi L_j d^2}{F_j \cos \theta_s} \quad (4)$$

where R_j , L_j and F_j are the at-sensor spectral reflectance, the spectral radiance and the mean solar exoatmospheric spectral irradiance (in $\text{W m}^{-2} \mu\text{m}^{-1}$) of the j th band, respectively. d is the earth–sun distance in astronomic units on the data acquisition day and θ_s is the solar zenith angle at the data acquisition time. To obtain a general conclusion on the consequence of the varieties of NDVI definitions from the intercomparison for various sensors, we considered the NDVI calculated only at the level of sensor in the following discussion because atmospheric conditions are time dependent and unpredictable. In addition, the atmospheric correction for the DN value is non-physical because the DN value is not a physical quantity. For the specific case where the atmospheric condition can be quantified, the NDVI at the ground surface corrected for atmospheric effects should always be pursued (see section 3.3). Our emphasis below is on the consequence and difference due to the various definitions of the NDVI and thus the necessity of optimizing the NDVI definitions for remote sensing of vegetation.

From table 1, we can see that different sensors have different ways of converting the DN value to spectral radiance. For ALI, conversion to spectral radiance takes different forms for products before 22 December 2004 compared with those on or after 22 December 2004. For ETM+ of Landsat 7, equation (T4) is for the Level 1 Product Generation System (LPGS) products ordered from the Earth Observation System (EOS) Data Gateway and National Land Archive Production System (NLAPS) products after 5 April 2004 ordered from Earth Explorer; equation (T5) is for the NLAPS products before 5 April 2004. $L_{\max,j}$ and $L_{\min,j}$ are, respectively, the maximum and minimum spectral radiances corresponding to the j th band, which should be found in the image header file accompanying the science data ordered.

Table 2 shows the relationships between NDVI_L and DN values. The bounded range for NDVI_{DN} is still between -1 and 1 , but the NDVI_L derived from the DN values can now be >1 or <-1 . For instance, for ALI data collected on or after 22 December 2004, for $\text{DN}_{\text{nir}} \in [0, 195]$ and $\text{DN}_r \in [0, 120]$ (along the line $0.61111\text{DN}_{\text{nir}} + \text{DN}_r - 119.44 = 0$, see table 2 for ALI), NDVI_L varies between $-20\ 169$ and $30\ 764$. Here $\text{DN}_{\text{nir}} \in [0, 195]$ denotes any DN value of the near-infrared band in the range between 0 and 195, and $\text{DN}_r \in [0, 120]$ denotes any DN value of the red band in the range between 0 and 120. For the 16-bit integer DN values of ALI, the area with $\text{DN}_{\text{nir}} \in [0, 195]$ and $\text{DN}_r \in [0, 120]$ corresponds to very dark targets such as dark soils (Huete and Tucker 1991), ocean and dark forest targets (Roderick *et al.* 1996). As pointed out by Roderick *et al.* (1996), NDVI values over darker targets are expected to be more sensitive to signal quantization and system noise. Therefore, it is difficult to use the NDVI_L in areas where both DN_{nir} and DN_r are too small to differentiate the types of land surface. The area

Table 2. Lookup table for calculation of NDVI_L from DN values.

Sensor	Relationship between NDVI _{DN} and NDVI _L	Notes
ALI	T9: NDVI _L = NDVI _{DN} (before 22 December 2004) T10: NDVI _L = $\frac{0.61111DN_{nir} - DN_r + 25}{0.61111DN_{nir} + DN_r - 119.44}$ (on or after 22 December 2004)	For ALI, bands 3 and 4 are used Blackout area is: DN _{nir} =0 and DN _r =0 (before 22 December 2004); DN _{nir} ∈ [0, 195] and DN _r ∈ [0, 120] (on or after 22 December 2004)
ASTER	T11: NDVI _L = $\frac{0.59746DN_{nir} - DN_r + 0.40254}{0.59746DN_{nir} + DN_r - 1.59746}$ T12: NDVI _L = $\frac{0.60919DN_{nir} - DN_r + 0.39081}{0.60919DN_{nir} + DN_r - 1.60919}$ T13: NDVI _L = $\frac{0.60847DN_{nir} - DN_r + 0.39153}{0.60847DN_{nir} + DN_r - 1.60847}$	For ASTER, bands 2 and 3 are used T11: for HG mode T12: for NG mode T13: for LG mode Blackout area: DN _{nir} ∈ [0, 3] and DN _r ∈ [0, 2] for all three gain modes
ETM+	T14: NDVI _L = $\frac{G \cdot DN_{nir} - DN_r - (G-1) + 254H_1}{G \cdot DN_{nir} + DN_r - (G+1) + 254H_2}$ T15: NDVI _L = $\frac{G \cdot DN_{nir} - DN_r + 255H_1}{G \cdot DN_{nir} + DN_r + 255H_2}$ where $G = \frac{L_{max,nir} - L_{min,nir}}{L_{max,r} - L_{min,r}}, H_1 = \frac{L_{min,nir} - L_{min,r}}{L_{max,r} - L_{min,r}} \text{ and}$ $H_2 = \frac{L_{min,nir} + L_{min,r}}{L_{max,r} - L_{min,r}}$	Equation (T14) is for LPGS products and NLAPS products after 5 April 2004 Equation (T15) is for NLAPS products before 5 April 2004 <i>L</i> _{max,j} and <i>L</i> _{min,j} should be found from the <i>Landsat-7 Science Data User's Handbook</i> when the operating modes of bands 3 and 4 are certified Blackout area for ETM+ is variable, depending on the operating modes of band 3 and 4 of a specific image
HRVIR	T16: NDVI _L = $\frac{1.48885DN_{nir} - DN_r}{1.48885DN_{nir} + DN_r}$	For HRVIR, bands 2 and 3 are used in calculating NDVI Blackout area: DN _{nir} =0 and DN _r =0
Hyperion	T17: NDVI _L = NDVI _{DN}	Blackout area: DN _{nir} =0 and DN _r =0
IKONOS	T18: NDVI _L = $\frac{0.77664DN_{nir} - DN_r}{0.77664DN_{nir} + DN_r}$ (before 22 February 2001) T19: NDVI _L = $\frac{0.77646DN_{nir} - DN_r}{0.77646DN_{nir} + DN_r}$ (after 22 February 2001)	For IKONOS, bands 3 and 4 are used Blackout area: DN _{nir} =0 and DN _r =0

where both DN_{nir} and DN_r are small and the resultant $|NDVI_L| \geq 1$ is referred to as a blackout area in the following discussion. The blackout areas for the calculation of the $NDVI_L$ with each sensor studied in this paper are shown in table 2.

2.1 Difference between $NDVI_L$ and $NDVI_{DN}$

For ALI data collected before 22 December 2004, $NDVI_L$ and $NDVI_{DN}$ are equal. However, for the data collected on or after 22 December 2004, the difference between $NDVI_L$ and $NDVI_{DN}$ for any possible combination of DN values for the nir and red bands is shown in figure 1(a), where the blackout area is excluded. From figure 1(a) we can see that for ALI, the $NDVI$ calculated using the spectral radiance is always smaller than that calculated using the DN value so that $NDVI_L - NDVI_{DN}$ is always negative. The difference can be as large as 0.31.

For ASTER data (see tables 1 and 2), the $NDVI_L$ is calculated using equations (T11)–(T13), based on whether the data are acquired with bands 2 (red band) and 3 (nir band) being operated in high gain (HG), normal gain (NG) or low gain (LG) mode. For the data collected in any of the gain modes, the blackout area is the same, that is $DN_{nir} \in [0, 3]$ and $DN_r \in [0, 2]$ (see table 2). The difference between $NDVI_L$ and $NDVI_{DN}$ for any possible combination of DN values of nir and red bands is

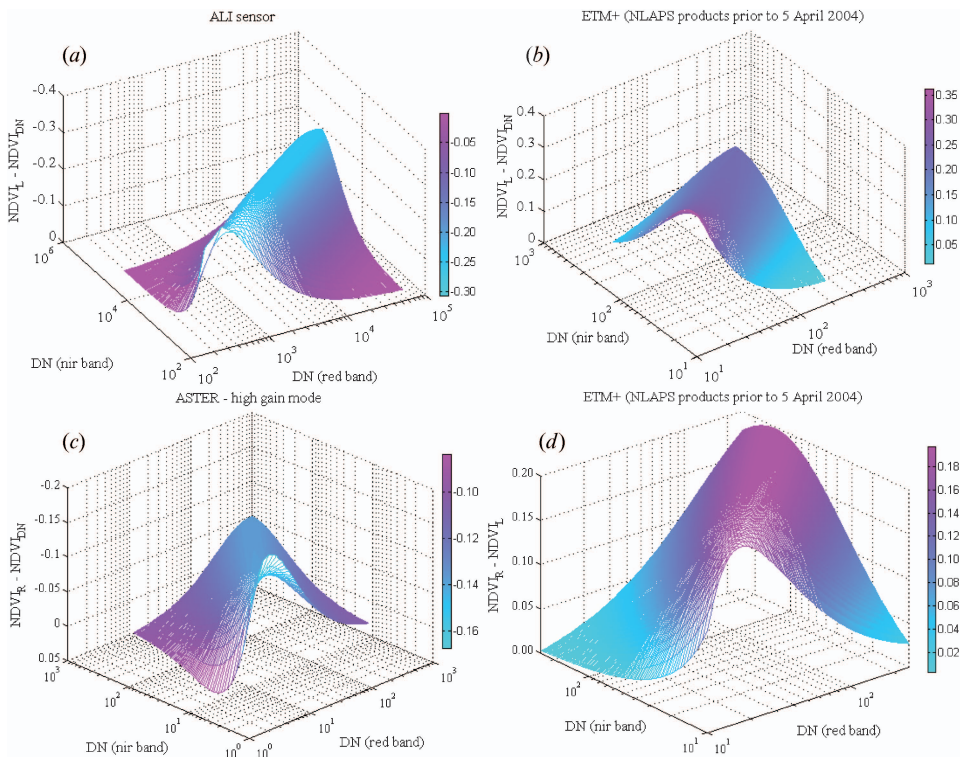


Figure 1. The difference between $NDVI_L$ and $NDVI_{DN}$ (a and b), $NDVI_R$ and $NDVI_{DN}$ (c) and $NDVI_R$ and $NDVI_L$ (d) for any combination of DN values of near-infrared and red bands for (a) ALI (16-bit), (b) ETM+ NLAPS products (8-bit) prior to 5 April 2004, (c) ASTER (high gain mode) and (d) ETM+ NLAPS products (8-bit) prior to 5 April 2004. The results for ETM+ LPGS products and NLAPS products after 5 April 2004 are very similar (not shown).

very similar to that for ALI data collected on or after 22 December 2004; $NDVI_L$ is always smaller than $NDVI_{DN}$ in the area where the blackout area is excluded, but the difference can be as high as 0.29 (HG mode) and 0.28 (both NG and LG modes).

For the ETM+ of Landsat 7 (see tables 1 and 2), there are two calibration modes available from radiances into DN; the LG and HG modes are selected according to the time of year (the sun's position) and the average albedo of the Landsat scene. Bands 3 and 4 were used in calculating the NDVI. The conversion formulae from DN values to spectral radiance are shown in table 2 for both LPGS and NLAPS products. Equations (T14) and (T15) for ETM+ in table 2 are general forms used in calculating $NDVI_L$ from DN values. As the operating modes of bands 3 and 4 can be different (for instance, bands 3 and 4 can both be in the HG mode or band 3 can be in the HG mode, to enhance data in vegetated area, but band 4 can be in the LG mode, to prevent saturation in actively vegetated zone), a specific formula has to be found for a specific image with $L_{max,j}$ and $L_{min,j}$ to be found from the image header file, or at least the operating modes of bands 3 and 4 are known from the image header file. As an example, let us consider ETM+ images acquired after 1 July 2000. If band 3 is in the HG mode and band 4 is in the LG mode, then $L_{max,nir}=241.1$, $L_{min,nir}=-5.1$, $L_{max,r}=152.9$ and $L_{min,r}=-5.0 \text{ W m}^{-2} \text{ sr}^{-1} \mu\text{m}^{-1}$ (NASA 2006). Equations (T14) and (T15) in table 2 become:

$$NDVI_L = \frac{1.55922DN_{nir} - DN_r - 0.72}{1.55922DN_{nir} + DN_r - 18.8063} \quad (5)$$

$$NDVI_L = \frac{1.55922DN_{nir} - DN_r - 0.16142}{1.55922DN_{nir} + DN_r - 16.3111} \quad (6)$$

where equation (5) is for the LPGS products and NLAPS products after 5 April 2004, and equation (6) is for the NLAPS products before 5 April 2004. The blackout area is $DN_{nir} \in [0, 10]$ and $DN_r \in [0, 17]$ for equation (5), slightly smaller than that of $DN_{nir} \in [0, 12]$ and $DN_r \in [0, 19]$ for equation (6). The difference between $NDVI_L$ and $NDVI_{DN}$ for any possible combination of DN values of nir and red bands for the NLAPS products prior to 5 April 2004 is shown in figure 1(b), where the blackout area is excluded. The differences between $NDVI_L$ and $NDVI_{DN}$ for the LPGS products and the NLAPS products after 5 April 2004 are very similar. The maximum difference is 0.36 for the LPGS and NLAPS products after 5 April 2004 and 0.34 for the NLAPS products prior to 5 April 2004. Figure 2(a) is a false colour image (RGB=bands 4, 3 and 2) of an ETM+ DN image acquired on 6 May 2002 in central-western New Mexico, USA (WRS path 34 row 36). Band 3 (red band) was in HG mode while band 4 (nir band) was in LG mode when this image was acquired. The red linear feature on the right running from south to north is the Rio Grande corridor. Along the Rio Grande River, the cottonwood (*Populus fremontii*) and saltcedar (*Tamarix* spp.) are dense. The dark red patches in the image are mountainous forests. In the northeast corner and to the east of the Rio Grande River lies Albuquerque city. This image was generated by the NLAPS processing system. Figure 2(b) shows the $(NDVI_L - NDVI_{DN})$ image generated from the raw DN ETM+ image using equation (6). As expected from figure 1(b), $NDVI_L$ is always greater than $NDVI_{DN}$; the difference varies between 0 and 0.28. No blackout area exists in this image. The NDVI is mainly used to study vegetation and we expect that the NDVI should not be sensitive to the definitions. However, the areas that have the largest values of $(NDVI_L - NDVI_{DN})$ (see figure 2(b)) correspond to

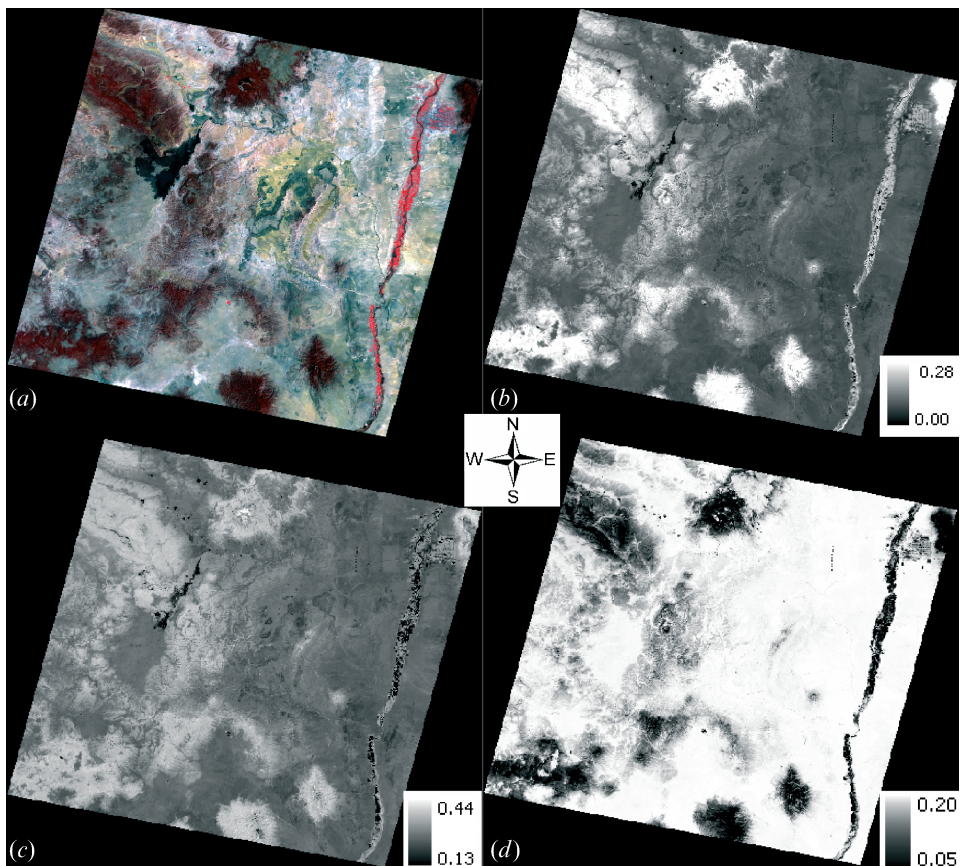


Figure 2. (a) False colour image (RGB=bands 4, 3 and 2) of ETM+ of Landsat 7 acquired on 6 May 2002 in central-western New Mexico, USA. (b) Image of $NDVI_L - NDVI_{DN}$ derived from the raw DN image for the same area as (a). (c) Image of $NDVI_R - NDVI_{DN}$ derived from the raw DN image. (d) Image of $NDVI_R - NDVI_L$ derived from raw DN image using equations (6) and (8).

vegetated areas, especially in the darker forest regions (figure 2(a)). These results may indicate that, for ETM+, NDVI definitions using spectral radiance and DN values are inconsistent.

For the HRVIR sensor onboard SPOT, the blackout area is $DN_{nir}=0$ and $DN_r=0$ (table 2). The difference between $NDVI_L$ and $NDVI_{DN}$ for any possible combination of DN values of nir and red bands is very similar to that of ETM+ shown in figure 1(b): $NDVI_L$ is always greater than $NDVI_{DN}$. The largest difference is 0.20.

For Hyperion, the blackout area is $DN_{nir}=0$ and $DN_r=0$ (table 2). The calibration relationship is given by equation (T7) in table 1, that is $L_{ij}=DN_{ij}/40$. Inserting this into equation (2) and comparing it with equation (1), we arrived at $NDVI_L=NDVI_{DN}$. This demonstrates that, for Hyperion, the NDVI defined by DN and radiance is the same. Hyperion is the only sensor in table 2 that was calibrated in this way.

For IKONOS, the blackout area is $DN_{nir}=0$ and $DN_r=0$ (table 2), similar to HRVIR and Hyperion. The difference between $NDVI_L$ and $NDVI_{DN}$ for any possible combination of DN values of the nir and red bands is similar to that of ALI shown in figure 1(a), except that the dynamic range is 11-bit rather than 16-bit as of ALI;

NDVI_L is always smaller than NDVI_{DN}. The largest difference in magnitude is 0.17. There is little difference between the products before and after 22 February 2001.

In summary: (1) NDVI_L is always greater than NDVI_{DN} for ALI, ASTER and IKONOS, it is always smaller than NDVI_{DN} for ETM+ and HRVIR, and it is equal to NDVI_{DN} for Hyperion; (2) in general, the difference between the NDVI calculated from DN values and that from radiance cannot be neglected, especially in vegetated areas.

2.2 Difference between NDVI_R and NDVI_{DN}

NDVI defined by spectral reflectance (equation (3)) can eventually be expressed in DN values by inserting equation (4) in equation (3), with the spectral radiance given by the formulae in table 1 in terms of DN values for various sensors. The resulted NDVI_R and the exoatmospheric spectral irradiance of each band used in the calculation of the NDVI_R for the sensors given in tables 1 and 2 are given in table 3. The blackout area for the NDVI_R calculation for each sensor is also given in table 3.

For the ALI sensor, spectral irradiances for bands 3 (r) and 4 (nir) are $F_r = 1551.47 \text{ W m}^{-2} \mu\text{m}^{-1}$ and $F_{nir} = 1164.53 \text{ W m}^{-2} \mu\text{m}^{-1}$, respectively. For data acquired before 22 February 2004, the NDVI_R from planetary spectral reflectance is given by equation (T20), which is similar to equation (6). For any possible combination of DN values of nir and red bands, the shape of NDVI_R - NDVI_{DN} is similar to that of figure 1(b): NDVI_R is always greater than NDVI_{DN}. The maximum difference is 0.14. The blackout area for this case is $DN_{nir} = 0$ and $DN_r = 0$. For data acquired on and after 22 February 2004, the NDVI_R is calculated using equation (T21) in table 3, which is similar to equation (T11) in table 2. The blackout area is $DN_{nir} \in [0, 165]$ and $DN_r \in [0, 136]$. For any possible combination of DN values of nir and red bands, NDVI_R - NDVI_{DN} is shown in figure 1(c), where the blackout area is excluded. For the combinations that $DN_r \geq 21\,698$ and $DN_{nir} > 23\,118$, NDVI_R is always smaller than NDVI_{DN}, but for other combinations NDVI_R can be larger than NDVI_{DN}. The maximum magnitude of difference is 0.23.

For ASTER, NDVI_R can be calculated using equations (T22)–(T24), depending on whether bands 2 and 3 operate in HG, NG or LG modes. For any gain mode and any possible combination of DN values of nir and red bands, NDVI_R - NDVI_{DN} is similar to that shown in figure 1(c). For most of the combinations, NDVI_R is smaller than NDVI_{DN}, but for combinations in the areas $DN_{nir} \leq 73$ and $DN_r \leq 94$ for the HG mode, $DN_{nir} \leq 66$ and $DN_r \leq 94$ for the NG mode, $DN_{nir} \leq 72$ and $DN_r \leq 95$ for the LG mode, NDVI_R can be larger than NDVI_{DN}. This means that in the lower reflective regions for bands 2 and 3 of ASTER, NDVI_R can be larger than NDVI_{DN}. The maximum magnitude of difference is 0.17 (HG) and 0.16 (NG and LG).

For ETM+, the conversion formulae from DN values to spectral reflectance are shown in table 3 for both LPGS and NLAPS products. Let us also consider ETM+ images acquired after 1 July 2000. If band 3 is in HG mode and band 4 is in LG mode, the corresponding equations for the NDVI from spectral reflectance become:

$$NDVI_R = \frac{2.31642DN_{nir} - DN_r - 5.4617}{2.31642DN_{nir} + DN_r - 23.5475} \quad (7)$$

$$NDVI_R = \frac{2.31642DN_{nir} - DN_r - 4.1616}{2.31642DN_{nir} + DN_r - 20.3108} \quad (8)$$

where equation (7) is for the LPGS and NLAPS products after 5 April 2004 and

Table 3. Lookup table for calculation of NDVI_R from DN values.

Sensor	Relationship between NDVI _{DN} and NDVI _L	Exoatmospheric irradiance (W m ⁻² μm ⁻¹) and blackout area
ALI	T20: NDVI _R = $\frac{1.33227DN_{nir} - DN_r}{1.33227DN_{nir} + DN_r}$ (before 22 December 2004) T21: NDVI _R = $\frac{0.81417DN_{nir} - DN_r + 9.309}{0.81417DN_{nir} + DN_r - 135.135}$ (on or after 22 December 2004)	For ALI, bands 3 (r) and 4 (nir) are used $F_{nir} = 1164.53$, $F_r = 1551.47$ Blackout area: $DN_{nir} = 0$ and $DN_r = 0$ (before 22 December 2004); $DN_{nir} \in [0, 165]$ and $DN_r \in [0, 136]$ (on or after 22 December 2004)
ASTER	T22: NDVI _R = $\frac{0.83030DN_{nir} - DN_r + 0.1697}{0.83030DN_{nir} + DN_r - 1.8303}$ T23: NDVI _R = $\frac{0.84659DN_{nir} - DN_r + 0.15341}{0.84659DN_{nir} + DN_r - 1.84659}$ T24: NDVI _R = $\frac{0.84559DN_{nir} - DN_r + 0.15441}{0.84559DN_{nir} + DN_r - 1.84559}$	For ASTER, bands 2 (r) and 3 (nir) are used $F_{nir} = 1119.47$, $F_r = 1555.74$ T22: for HG mode T23: for NG mode T24: for LG mode Blackout area: $DN_{nir} \in [0, 3]$ and $DN_r \in [0, 2]$ for all three gain modes
ETM+	T25: NDVI _R = $\frac{G' \cdot DN_{nir} - DN_r - (G' - 1) + 254H'_1}{G' \cdot DN_{nir} + DN_r - (G' + 1) + 254H'_2}$ T26: NDVI _R = $\frac{G' \cdot DN_{nir} - DN_r + 255H'_1}{G' \cdot DN_{nir} + DN_r + 255H'_2}$ where $G' = 1.48563$ $\frac{L_{max, nir} - L_{min, nir}}{L_{max, r} - L_{min, r}}$, $H'_1 = \frac{1.48563L_{min, nir} - L_{min, r}}{L_{max, r} - L_{min, r}}$ and $H'_2 = \frac{1.48563L_{min, nir} + L_{min, r}}{L_{max, r} - L_{min, r}}$	For ETM+, bands 3 (r) and 4 (nir) are used $F_{nir} = 1044$, $F_r = 1551$ Equation (T25): for LPGS products and NLAPS products after 5 April 2004; Equation (T26): for NLAPS products before 5 April 2004 Blackout area for ETM+ is variable, depending on the operating modes of band 3 and 4 of a specific image
HRVIR	T27: NDVI _R = $\frac{2.21912DN_{nir} - DN_r}{2.21912DN_{nir} + DN_r}$	For HRVIR, bands 2 and 3 are used in calculating NDVI $F_{nir} = 1052$, $F_r = 1568$ Blackout area: $DN_{nir} = 0$ and $DN_r = 0$
Hyperion	T28: NDVI _R = $\frac{1.34218DN_{nir} - DN_r}{1.34218DN_{nir} + DN_r}$	For Hyperion, bands 33 (0.6812 μm) and 45 (0.8033 μm) are used in calculating NDVI $F_{nir} = 1131$, $F_r = 1518$ Blackout area: $DN_{nir} = 0$ and $DN_r = 0$
IKONOS	T29: NDVI _R = $\frac{1.03925DN_{nir} - DN_r}{1.03925DN_{nir} + DN_r}$ (before 22 February 2001) T30: NDVI _R = $\frac{1.03888DN_{nir} - DN_r}{1.03888DN_{nir} + DN_r}$ (after 22 February 2001)	For IKONOS, bands 3 and 4 are used in calculating NDVI $F_{nir} = 1148$, $F_r = 1536$ Blackout area: $DN_{nir} = 0$ and $DN_r = 0$

equation (8) is for the NLAPS products before 5 April 2004. The blackout area for equation (7) is $DN_{nir} \in [0, 10]$ and $DN_r \in [0, 23]$; and for equation (8) it is $DN_{nir} \in [0, 8]$ and $DN_r \in [0, 20]$. The difference between NDVI_R and NDVI_{DN} for any possible combination of DN values of nir and red bands (the blackout area is excluded) for the NLAPS products prior to 5 April 2004 (equation (8)) is similar to figure 1(b); NDVI_R is always greater than NDVI_{DN}, and the difference can be as high as 0.47. That for the LPGS products and the NLAPS products after 5 April

2004 (equation (7)) is very similar; $NDVI_R$ is always greater than $NDVI_{DN}$, and the maximum difference is also 0.47. A case study shown in figure 2(c) is the $(NDVI_R - NDVI_{DN})$ image generated from the raw DN ETM+ image (figure 2(a)) of central-western New Mexico. As expected, $NDVI_R$ is always greater than $NDVI_{DN}$ everywhere in the image. The difference varies between 0.13 and 0.44; no blackout area exists. Similar to the case of $(NDVI_L - NDVI_{DN})$ (see figure 2(b)), the areas that have largest values of $(NDVI_R - NDVI_{DN})$ correspond to vegetated areas, especially at the darker forest regions. These results also indicate that for ETM+, NDVIs defined using spectral reflectance and DN value are inconsistent, especially in vegetated areas.

For the HRVIR sensor onboard SPOT, $NDVI_R$ is always greater than $NDVI_{DN}$. The difference can be as high as 0.39. For Hyperion, $NDVI_R$ is always greater than $NDVI_{DN}$, with the maximum difference being 0.15. For IKONOS, $NDVI_R$ is always greater than $NDVI_{DN}$. However, the largest difference is 0.02 for products either before or after 22 February 2001.

In summary, we conclude that: (1) for ALI data acquired before 22 February 2004, $NDVI_R$ is always greater than $NDVI_{DN}$. The maximum difference is 0.14. For ALI data on or after 22 February 2004, $NDVI_R$ is always smaller than $NDVI_{DN}$ when $DN_r \geq 21698$ and $DN_{nir} \geq 23118$. In the lower reflective region where $DN_r < 21698$ and $DN_{nir} < 23118$, $NDVI_R$ can be larger than $NDVI_{DN}$. The maximum magnitude of difference is 0.23. (2) For ASTER data, if $DN_{nir} > 73$ and $DN_r > 94$ for the HG mode, $DN_{nir} > 66$ and $DN_r > 94$ for the NG mode, and $DN_{nir} > 72$ and $DN_r > 95$ for the LG mode, $NDVI_R$ is always smaller than $NDVI_{DN}$; but in the lower reflective regions for bands 2 and 3, $NDVI_R$ can be larger than $NDVI_{DN}$. The maximum magnitude of difference is 0.17 (HG) and 0.16 (NG and LG). (3) For ETM+ data, the conversion from DN values to spectral reflectance for LPGS and NLAPS products is given by equations (T25) and (T26) in table 3. Specific forms of these equations depend on the operating modes of bands 3 and 4. For the case that band 3 is in the HG mode and band 4 is in the LG mode, $NDVI_R$ is always greater than $NDVI_{DN}$ for both LPGS and NLAPS products, with the difference being as high as 0.47. The case study in central-western New Mexico shows that for ETM+, NDVIs defined using spectral reflectance and DN values are inconsistent. However, the difference is the largest in vegetated areas. (4) For HRVIR, $NDVI_R$ is always greater than $NDVI_{DN}$, with the maximum difference being 0.39. (5) For Hyperion data, $NDVI_R$ is always greater than $NDVI_{DN}$, with the maximum difference being 0.15. (6) For IKONOS, $NDVI_R$ is always greater than $NDVI_{DN}$ and the largest difference is 0.02. This demonstrates that, among the sensors studied, IKONOS is the only sensor calibrated in this way for which NDVI defined using spectral reflectance can be calculated using DN values directly without resulting in differences greater than 0.02.

2.3 Difference between $NDVI_R$ and $NDVI_L$

For ALI data acquired before 22 February 2004, $NDVI_R = NDVI_{DN}$. Thus, $NDVI_R - NDVI_L = NDVI_R - NDVI_{DN}$. As discussed in section 2.2, $NDVI_R$ is always greater than $NDVI_{DN}$. Therefore, for ALI data acquired before 22 February 2004, $NDVI_R$ is always greater than $NDVI_L$. The maximum difference is 0.14. For data acquired on and after 22 February 2004, $NDVI_R - NDVI_L$ is calculated using equations (T10) and (T21). The results show that for any combination of DN_r and DN_{nir} (similar to figure 1(b)), $NDVI_R - NDVI_L$ is always greater than zero, with the maximum difference being 0.14.

For ASTER data, the results show that $NDVI_R$ is always greater than $NDVI_L$ for any operating gain mode, with the maximum difference being 0.16.

As the calculation of both $NDVI_R$ and $NDVI_L$ for ETM+ depends on the operating gain mode of bands 3 and 4, we take as an example the case that band 3 is in HG mode and band 4 is in LG mode. For the NLAPS products before 5 April 2004, $NDVI_R$ and $NDVI_L$ are given by equations (8) and (6), respectively. For any combination of DN_r and DN_{nir} , $NDVI_R$ is always greater than $NDVI_L$, as shown in figure 1(d). The difference can be as high as 0.20. Compared with figure 1(b), figure 1(d) shows that higher values of $(NDVI_R - NDVI_L)$ appear at regions where DN_r is higher. As the vegetated area has low spectral reflectance at the red band, it is expected that in vegetated regions, $DN_r - DN_{nir}$ would be low. For the LPGS and NLAPS products after 5 April 2004, $NDVI_R$ and $NDVI_L$ are given by equations (7) and (5), respectively. For any combination of DN_r and DN_{nir} , $NDVI_R$ is always greater than $NDVI_L$, which is similar to figure 1(d). The maximum difference is also 0.20. A case study shown in figure 2(d) is the $(NDVI_R - NDVI_L)$ image generated from the raw DN ETM+ image (figure 2(a)) of central-western New Mexico. As expected, $NDVI_R$ is always greater than $NDVI_L$; thus $NDVI_R - NDVI_L$ is positive everywhere in the image. The difference varies between 0.05 and 0.20. Contrary to the cases of $(NDVI_L - NDVI_{DN})$ and $(NDVI_R - NDVI_{DN})$ (see figures 2(b)–2(c)), the areas that have lowest values correspond to vegetated areas, even though in most of the vegetated areas the difference is still greater than 0.14. For instance, a spatial profile retrieved from a polyline along the vegetated Rio Grande corridor (the dark linear feature to the right in figure 2(d)) shows that 85% (5890 pixels) of the 6938 pixels of the polyline have a value greater than 0.14. For other types of surface, the largest difference reaches the possible maximum value of 0.2. These results indicate that, for ETM+, NDVIs defined using spectral reflectance and radiance values are more consistent in vegetated areas than those defined using either spectral reflectance and DN values or spectral radiance and DN values, but the difference $(NDVI_R - NDVI_L)$ is still significant (>0.14).

For HRVIR data, $NDVI_R$ is always greater than $NDVI_L$, with the maximum difference being 0.20. Like the ETM+ data discussed above, there is a shift of positions of large difference $(NDVI_R - NDVI_L)$ to where DN_r is higher compared to the cases of $(NDVI_R - NDVI_{DN})$ and $(NDVI_L - NDVI_{DN})$. Thus, for HRVIR, it is also expected that, in vegetated areas, $DN_r - DN_{nir}$ is lower than in the other areas.

For all IKONOS data (before or after 22 February 2001), the difference $NDVI_L - NDVI_{DN}$ for any possible combination of DN values of nir and red bands is greater than zero, with the maximum difference being 0.15.

In summary, we conclude that: (1) for all of the sensors discussed, $NDVI_R$ is always greater than $NDVI_L$. The maximum differences are 0.14 (ALI), 0.15 (IKONOS), 0.16 (ASTER) and 0.20 (ETM+ and HRVIR). Using spectral radiance rather than spectral reflectance to calculate the NDVI defined by spectral reflectance will always underestimate the NDVI; (2) for vegetated areas, the difference between $NDVI_R$ and $NDVI_L$ is smaller than for other surface types, but is still significant.

2.4 Optimization of NDVI definitions

The above results show that the differences in NDVI between any two of the NDVI definitions using spectral reflectance, spectral radiance and DN values are significant, especially in vegetated areas. Therefore, it is necessary to optimize the NDVI definitions for consistency in data derived from different sensors and at different

times. Use of DN values or digital counts and spectral radiance should always be avoided because data from different sensors are generally different in radiometric resolutions and thus their respective values carry different levels of information and cannot be compared directly. In addition, the atmospheric correction to DN values is often difficult because the physics in the atmospheric correction to DN value is not clear and often confusing. As reflected spectral radiance is dependent on the incidental spectral radiance and atmospheric conditions, NDVIs derived from radiance measured at different times are difficult to compare. From a spectroscopic point of view, among the three radiative quantities used to define the NDVI, spectral reflectance is the only property of a material. Spectral reflectance from a specific pixel does not depend on the intensity of incident solar radiation, while spectral radiance and DN value do. Therefore, it is expected that NDVIs calculated using spectral reflectance would be different from those calculated using spectral radiance and DN values. The DN value depends not only on the intensity of the incident radiance but also on the analogue-to-digital (A/D) conversion and calibration of the specific sensor (information on gain and offset) of the two bands whose data are used for the NDVI calculation. If two bands of the same sensor have the same form of DN-to-radiance conversion (see equations (T1) and (T7) of table 1), the calculated NDVI using radiance and DN values is the same; otherwise, it is different.

In summary, using spectral reflectance to compute the NDVI will provide a sound basis for the intercomparison of NDVIs measured over time and by different sensors. Therefore, using spectral reflectance to define the NDVI or any other vegetation index should be encouraged, so that the NDVIs measured by different sensors and at different times are comparable and long-term data consistency can be guaranteed (Nouvellon *et al.* 2001, Thenkabail 2004).

3. Fractional vegetation coverage models

3.1 Modes for estimation of areal vegetation coverage

Spectral mixing analysis is a common method used to retrieve subpixel fractional vegetation cover (F) from remote sensing optical images (e.g. McGwire *et al.* 2000, Okin *et al.* 2001, Asner and Heidebrecht 2002, North 2002, Riaño *et al.* 2002, Coca *et al.* 2004). Spectral reflectance and vegetation indices are used to estimate F (Choudhury *et al.* 1994, Wittich and Hansing 1995, Carlson and Ripley 1997, Gillies *et al.* 1997, Gutman and Ignatov 1998, Leprieur *et al.* 2000, Qi *et al.* 2000, Zeng *et al.* 2000, Peterson *et al.* 2002, Lu *et al.* 2003, Ruiz and Garbn 2004). Most of these algorithms can be grouped into one of three common F models: the linear spectral mixing analysis model (referred to as the linear reflectance model) and two NDVI-based models, the linear NDVI model and the quadratic NDVI model. From the discussion in section 2, the NDVI should be defined in terms of spectral reflectance rather than spectral radiance or DN values. Thus, in the following discussion of F models, we only consider the NDVI defined in terms of spectral reflectance.

The linear reflectance model is a common method used to obtain fractional vegetation cover within a pixel (e.g. Smith *et al.* 1990a,b, Roberts *et al.* 1993, 1998, Asner and Heidebrecht 2002). The overall reflectance of a pixel of the i th band is defined as:

$$R_i = \sum_j (R_{ij} X_j) \quad (9)$$

with constraint equation

$$\sum_j X_j = 1 \quad (10)$$

where R_{ij} is the spectral reflectance of the j th endmember for band i , X_j the fractional surface area covered by the j th endmember, and R_i is the mixed reflectance of a ground pixel of band i . The fundamental physics for this model is that the reflected energy from a multicomponent surface collected by a spectroradiometer is a radiometrically decipherable (and thus linear) combination of the energy reflected from each component in proportion to its areal percentage, ignoring any non-linear effects. Thus, the spectral reflectance recorded for a ground pixel at any single band is the linear combination of the spectral reflectances of the surface features (endmembers) weighted according to their respective areal proportions (e.g. Adams *et al.* 1986, Karnieli *et al.* 2002).

Based on correlation analyses, Gertner *et al.* (2002) found that of seven tested non-linear multiband transformations of Landsat TM images, the NDVI has the highest correlation with F . Ünsalan and Boyer (2004) presented a theoretical justification of the NDVI as an indicator of surface vegetation characteristics. Table 4 shows some F -NDVI linear and quadratic models published. For simplicity, we categorize these NDVI-based models into the linear NDVI model and the quadratic NDVI model, respectively, depending on whether a model is a linear or a quadratic function of the NDVI. The linear NDVI model is expressed as (e.g. Wittich and Hansing 1995, Gutman and Ignatov 1998, Leprieur *et al.* 2000, Qi *et al.* 2000, Zeng *et al.* 2000, Lu *et al.* 2003):

$$F = \frac{\text{NDVI} - \text{NDVI}_0}{\text{NDVI}_\infty - \text{NDVI}_0} \quad (11)$$

and the quadratic NDVI model as (e.g. Choudhury *et al.* 1994, Carlson and Ripley 1997, Gillies *et al.* 1997):

$$F = \left(\frac{\text{NDVI} - \text{NDVI}_0}{\text{NDVI}_\infty - \text{NDVI}_0} \right)^2 \quad (12)$$

where NDVI_∞ is the NDVI of the surface 100% covered by green vegetation (or the NDVI of the 100% green vegetation endmember) and NDVI_0 is the NDVI of 100% bare soil surface (or the NDVI of the bare soil endmember). The linear NDVI model assumes that the pixel NDVI is the average of the NDVI of each endmember weighted by their areal fractions. The quadratic NDVI model assumes that the average is weighted by the square root of the areal fraction.

3.2 Spectral reflectance and endmember data collection

To compare the derived vegetation areal coverage from the three models as expressed by equations (9), (11) and (12) with *in situ* measurements, we first need to identify the endmembers, measure the spectral reflectance, measure the areal coverage of each endmember, and derive the NDVI distribution. To this end, the Sevilleta National Wildlife Refuge (NWR) in central New Mexico, USA was selected as the study site. As this site is in a semiarid region, the vegetation structure is relatively simple; there are two main types of vegetated surface, shrub land and woodland, with distinctive vegetation height and canopy leaf area index (LAI)

Table 4. Common NDVI-based models for deriving fractional vegetation coverage.

<i>F</i> -NDVI models	NDVI ₀	NDVI _∞	<i>F</i>	Surface types	Remote sensing image	Reference
$F=[N]$	0.10 fitted value	0.66 fitted value	Estimated from temporal phenological observations	Vineyard, grass, wheat field, western Germany	AVHRR	Wittich and Hansing 1995
$F=[N]$	0.04 estimated from GVI data (0.15°)	0.52 estimated from GVI data (0.15°)	No field measurements	Global, various	AVHRR	Gutman and Ignatov 1998
$F=[N]$	0.05	Estimated from the images	No field measurements	Global, various	AVHRR, TM	Zeng <i>et al.</i> 2000
$F=[M]$	0.20	0.72	Field measurements	Sahelian vegetation, Africa	AVHRR, SPOT	Leprieur <i>et al.</i> 2000
$F=[N]$	Implicitly estimated by linear regression		No field measurements	Australia	AVHRR	Lu <i>et al.</i> 2003
$F=[M] \cdot [N]$	Estimated from scatter plot of remote-sensed NDVI and surface temperature		Inversed from SVAT model	FIFE site in Kansas, USA; MONSOON'90 at Walnut Gulch in Arizona, USA	AVHRR, NS001	Gillies <i>et al.</i> 1997
$F=1-(1-[N])^m$ $m=0.5-0.75$, also referred to as $F=[M] \cdot [N]$	Relationship estimated from a heat balance and a radiative transfer model					Choudhury <i>et al.</i> 1994
$F=[M] \cdot [N]$	Derived from a radiative transfer model					Carlson and Ripley 1997

$[N]=[(NDVI-NDVI_0)/(NDVI_\infty-NDVI_0)]$, where NDVI_∞ represents the NDVI of the surface 100% covered by green vegetation, and NDVI₀ is the NDVI of 100% bare soil surface. Gillies *et al.* (1997) and Carlson and Ripley (1997) referred to Choudhury *et al.*'s (1994) results as $F=[N] \cdot [N]$, which could be more or less observed from Choudhury's data.

(Hobbie *et al.* 2003). Measurements and observation were thus carried out in two biomass zones: shrubland in a relatively flat area of the refuge, which represents a biomass zone of low LAI; and piñon-juniper woodland along the eastern slope of Los Pinos Mountains, which represents a biomass zone of high LAI. Endmembers in the shrub biomass zone include creosote shrub and bare soil. Measurements and observations in the shrub biomass were selected in an area of 304 594 m² (or 375 pixels of an ETM+ image), representing 'uniform' stands of shrub. The creosote shrub is about 1 m in height and 1 m in diameter. The LAI is approximately equal to 1. As the piñon-juniper biomass zone has a visible difference in species richness, we selected two plots, one with high *F* and the other with lower *F* for field measurements, each plot representing relatively 'uniform' stands and covering an area of 304 594 m² (or 375 pixels of an ETM+ image). The endmember spectrum and ground vegetation areal fraction measurements were sampled randomly within these three selected plots. The endmembers in the woodland biomass zone include piñon, juniper and soil. The tree height varies with an estimated mean of 4 m, and the crown diameter varies with a measured mean of 2.3 m. The canopy LAI was estimated to vary between 3 and 8.

The spectral reflectance of all endmembers (piñon, juniper, creosote shrub, soils, and shadow on soil) were measured using a portable hyperspectral spectroradiometer (model FieldSpec[®]Pro FR, Analytical Spectral Devices, Inc., Boulder, CO, USA) in the same season as the acquisition of a Landsat ETM+ image (16 June 2002; WRS path 33 row 36). The field of view of the fore-optic sensor is about 25°. Measurements were carried out under clear-sky conditions around noon (± 2 h), at a height between 1 and 2 m above the ground. The fore-optic sensor was placed 2–5 cm above the arbitrarily selected point of the target. The viewing direction of the sensor was in nadir (similar to ETM+). Spectral radiance data were collected for each endmember and a white reference panel (Spectralon, Labsphere, NH, USA) so that the spectral reflectance was obtained as the ratio of the spectral radiance data of the endmember to that of the reference panel. For each vegetation endmember, measurements were taken for 3–5 shrubs. For each shrub, usually 20–50 samples were taken; all individuals and samples were randomly selected on the sunlit side. The mean taken from all the measurements for each endmember was then used as the representative endmember spectrum for the spectral unmixing analysis.

To measure the fractional vegetation cover in the piñon-juniper biomass zone, seven ground cells with the same size as an ETM+ pixel (28.5 m \times 28.5 m) were randomly selected, four in one plot with higher *F* and three in the other plot with lower *F*. As the effective field of view for both our field optical measurement and ETM+ sensor is almost vertical, the deformation in the vegetation area due to viewing angle and topography was therefore neglected. The crown diameter of each individual tree within each cell was measured, and used to estimate the crown area by vertical projection. Specifically, the edge of the crown was projected vertically onto the ground and several distances across the tree trunk were measured and the average was taken as the crown diameter. Then the crown area of the tree was calculated as the vertically projected area on the ground. The fractional vegetation cover of each cell was then calculated by summing the crown areas and dividing by the cell area. The shrub-crown cover fraction of shrub biomass was measured using a similar vertical projection method as reported elsewhere (Kurc and Small 2004). Piñon and juniper in the piñon-juniper biomass zone were treated as one endmember because of their similarity in spectral reflectance (McGwire *et al.* 2000).

3.3 Atmospheric and topographic corrections

The spectral radiance corresponding to each pixel in an image acquired from a satellite sensor includes the reflected spectral radiance from the surface target and the path radiance due to the scattering of atmosphere. To calculate the NDVI at the ground surface, the original Landsat ETM+ DN image (16 June 2002; WRS path33 row36) was first converted to spectral radiance L at the sensor (section 2), and then atmospherically corrected using the dark object subtraction (DOS) method (Chavez 1996, Song *et al.* 2001) to obtain the surface spectral reflectance $R_{j,s}$ of the j th band:

$$R_{j,s} = \frac{\pi(L_j - L_{p,j})d^2}{T_{u,j}(T_{d,j}F_j \cos \theta_s + F_{d,j})} \tag{13}$$

where $T_{u,j}$ ($T_{d,j}$) is the upwelling (downwelling) transmittance of the atmosphere at the j th band. $F_{d,j}$ is the downwelling diffuse irradiance due to atmospheric scattering. $L_{p,j}$ is the path spectral radiance and is given as:

$$L_{p,j} = L_{\min,j} - \frac{R_{s,j}^{DO}(T_{d,j}F_j \cos \theta_s + F_{d,j})T_{u,j}}{\pi} \tag{14}$$

where $L_{\min,j}$ is the minimum spectral radiance in the image of the j th band, corresponding to the dark object (DO) whose surface spectral reflectance is $R_{s,j}^{DO}$, which is generally takes as 0.01. In the DOS method, $T_{u,j}$ and $T_{d,j}$ are approximated by the cosine of the solar and viewing zenith angles, respectively, assuming that there is very little diffuse downwelling irradiance (Moran *et al.* 1992, Chavez 1996, Song *et al.* 2001, Soudani *et al.* 2006).

The topography affects the solar incident angle, and thus the spectral radiance. A digital elevation model (DEM) of 30 m × 30 m resolution was applied to correct for the effect of slope angle and aspect using an algorithm developed by Duffie and Beckman (1991).

3.4 Comparison of modelled results with *in situ* measurement

The linear reflectance model was used to obtain the fractional vegetation cover by unmixing analysis. Shadow (darkness cast on one endmember due to another, e.g. vegetation shadow on soil) and shade (darkness cast within the endmember, e.g. some leaves in shadow of other leaves) change the reflected radiance from a pixel.

First, we estimated the shadow fraction so that we could use the endmember spectral reflectance and surface coverage to compare the modelled results with *in situ* measurements. Three endmembers (vegetation, bare soil, and shadow on soil) were used in the linear reflectance model. To estimate the shadow effect, the derived vegetation fractions from the linear reflectance model with and without the shadow endmember were compared with each other and also with the measurement.

For shadow corrections due to the oblique solar position, we assumed that (a) the solar shadow of the vegetation falls on the intercanopy space, and (b) the cross-section of a vegetation crown has a shape between a triangle and a rectangle. The solar shadow factor (SF) of vegetation, which is defined as the ratio of the actual or effective shadow area of vegetation to the vertically projected canopy area (see figure 3), is thus given by:

$$SF = \frac{A_{\text{shadow}}}{A_{\text{canopy}}} \tag{15}$$

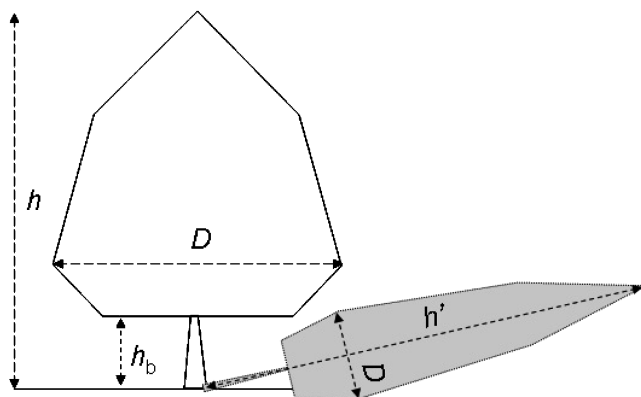


Figure 3. The tree shadow caused by the oblique solar position.

where A_{shadow} and A_{canopy} are the effective shadow area and vertically projected canopy area, respectively. Assuming the vegetation height is h , the height of the trunk below the vegetation crown is h_b , the diameter of the vertical projection of the vegetation crown is D , and the solar zenith angle is θ , then:

$$A_{\text{canopy}} = \pi \left(\frac{D}{2} \right)^2 \quad (16)$$

For Landsat ETM+, the viewing geometry is in nadir, thus the shadow is mainly determined by the solar zenith angle once the tree geometry is specified. From figure 3, if the shadow is within the vertically projected canopy area, the shadow area is zero, that is:

$$A_{\text{shadow}} = 0, \quad \text{if } h \tan \theta \leq (D/2) \quad (17)$$

Otherwise, the effective shadow area is the theoretical shadow area (projected area from solar ray direction) subtracted by the part that overlaps with the vertically projected canopy area. The respective altitude is $(h \tan \theta - D/2)$ if the shadow overlaps with the crown vertical projection, or $(h \tan \theta - h_b \tan \theta)$ if not. Combining these two situations, we have:

$$A_{\text{shadow}} = \frac{3}{4} \left(h \tan \theta - \max \left(h_b \tan \theta, \frac{D}{2} \right) \right) D, \quad \text{if } h \tan \theta > (D/2) \quad (18)$$

Inserting equations (16)–(18) into equation (15), we have:

$$\text{SF} = \begin{cases} \frac{\frac{3}{4} (h \tan \theta - \max(h_b \tan \theta, \frac{D}{2})) D}{\pi (\frac{D}{2})^2}, & \text{for } h \tan \theta > D/2, \\ 0, & \text{for } h \tan \theta \leq D/2, \end{cases} \quad (19)$$

The SF correction factor depends on the canopy geometry, specifically the canopy aspect ratio (h/D). For example, SF varies from 0, 0.15, 0.37 to 0.58 for an aspect ratio (h/D) of 1, 1.5, 2 and 2.5, respectively. In the shrub biomass zone discussed in the text, the canopy aspect ratio is around 1, the shadow effect is very small because SF is near zero. For the woodland sites, it is difficult to assign an accurate SF for the woodland sites where piñon and juniper have different canopy aspect ratios and the proportions of the two vegetation types vary with the pixels. We used an average canopy diameter of 2 metres, and an average canopy height of 4 metres, estimated

from the observations of seven field pixels. For the above shadow correction method (equation 19) to be transferable to other sites, basic vegetation characteristics such as individual tree height, height of the trunk below the vegetation crown, and the diameter of the vertical projection of the vegetation crown need to be known. To obtain the best results, this model may apply only to situations where canopy shadows are not intercepted by neighbouring canopies.

Using the field-measured spectral reflectance for the endmembers (vegetation, shadow of vegetation on soil, and soil) in equations (11) and (12), the linear and quadratic NDVI models were applied to estimate the fractional vegetation cover for each pixel. The mean fractional vegetation cover for all of the pixels in each plot (375 pixels) is taken as the representative fractional vegetation cover F for the plot. The derived F from the three models was then compared to the field-measured F for each plot in table 5.

The measured mean spectral reflectances of the surface endmembers for each biomass zone are shown in figure 4 and are taken as the representative spectral reflectance of each endmember in the biomass zone. The derived (see equation (3)) NDVI is 0.748 and 0.077 for the shrub and intershrub soil, respectively, in the shrub biomass zone; and 0.766 and 0.069 for the piñon-juniper and intercanopy soil, respectively, in the piñon-juniper biomass zone. As discussed in section 3.2, the mean fractional vegetation cover of each sample cell was calculated by summing the crown areas and dividing by the cell area. The measured mean fractional vegetation coverage for each plot (304 594 m²) was taken as the average of the mean fractional vegetation cover of each cell, for all cells sampled. The measured mean fractional vegetation coverage in the shrub biomass zone (plot 1) was about 0.30. Those for the dense piñon-juniper plot (plot 2) and the less dense piñon-juniper plot (plot 3) in the piñon-juniper biomass zone are 0.33 and 0.21, respectively (see table 5).

Table 5. Comparison of the fractional vegetation coverage for each plot (area=304 594 m²) in the shrub biomass zone (plot 1) and woodland biomass zone (plots 2 and 3) obtained from field measurements and derived from the linear reflectance (LR), linear NDVI (LN) and quadratic NDVI models (QN).

	Statistics	Field*	LR ₁	LR ₂	LN	QN
Shrub biomass zone (plot 1)	Mean	0.30	0.306	0.306	0.117	0.014
	Standard deviation		0.026	0.026	0.012	0.003
	Minimum		0.227	0.227	0.081	0.007
	Maximum		0.376	0.376	0.155	0.024
Woodland biomass zone (plots 2 and 3)	Mean	0.33	0.448	0.355	0.318	0.103
	Standard deviation		0.067	0.053	0.044	0.028
	Minimum		0.285	0.226	0.201	0.040
	Maximum		0.610	0.488	0.443	0.197
	Mean	0.21	0.340	0.274	0.194	0.039
	Standard deviation		0.066	0.053	0.036	0.015
	Minimum		0.174	0.139	0.083	0.007
	Maximum		0.500	0.407	0.304	0.093

LR₁, linear reflectance model without shadow-effect correction (two endmembers: soil, vegetation); LR₂, linear reflectance model with shadow-effect correction (three endmembers: soil, vegetation, and shadow).

*Field-measured F (the number of tree stands or tree clusters) of 0.27 (67), 0.30 (68), 0.40 (82) and 0.33 (56) in plot 2, and 0.21 (21), 0.26 (39) and 0.17 (25) in plot 3 of the woodland biomass, respectively.

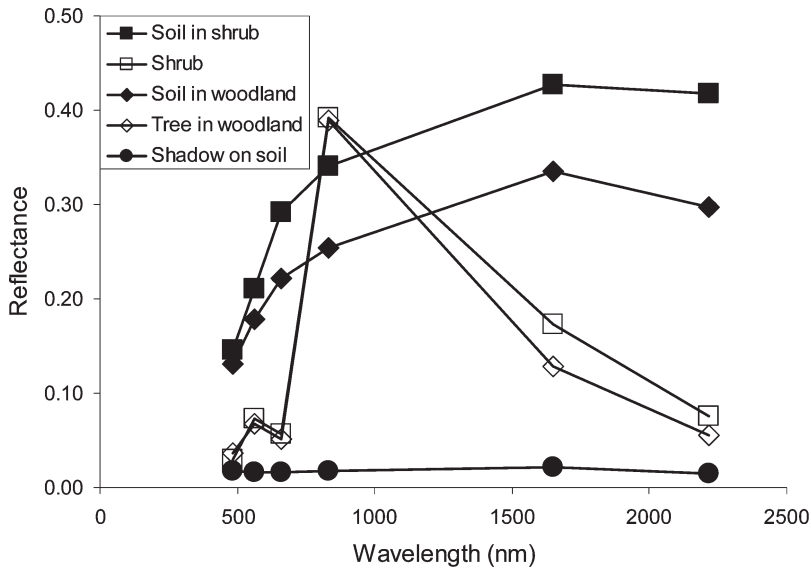


Figure 4. Field-measured reflectance spectra of the surface endmembers at six ETM+ bands.

The fractional vegetation coverage was also derived from the pixel spectral reflectance (for the linear reflectance model) and pixel NDVI (for the two NDVI-based fraction models) for all pixels (375 pixels) in each plot. The average fractional vegetation coverage for each plot is the mean fractional vegetation coverage of all pixels in the plot and is given in table 5. The linear reflectance model gives the largest F , while the quadratic NDVI model gives the lowest for all three plots. In the shrub biomass zone (plot 1), the linear reflectance model gives a mean fractional vegetation cover of 0.306, which agrees well with the field measurement ($F=0.30$). The shadow effect in the linear reflectance model is not visible for plot 1. Both linear ($F=0.117$) and quadratic ($F=0.014$) NDVI models underestimate the fractional vegetation coverage as compared with our field measurements. In the piñon-juniper biomass zone, the linear NDVI model gives the best agreement with the measurement (0.318 of model versus 0.33 of measurement for plot 2; 0.194 of model versus 0.21 of measurement for plot 3). The linear reflectance model with shadow effect corrected overestimates the F (0.355 of model versus 0.33 of measurement for plot 2; 0.274 of model versus 0.21 of measurement for plot 3), while if shadow effect is not corrected, it overestimates the F by more (0.448 of model versus 0.33 of measurement for plot 2; 0.340 of model versus 0.21 for plot 3). In both plots in the woodland biomass zone, the quadratic NDVI model underestimates F . A detailed comparison of the seven field data sets (cells) with the model-derived F of the respective pixels is shown in figure 5. The conclusion of the relative performance of the models is the same as that drawn from table 5: in the woodland biomass zone, the linear NDVI model outperforms the other two models.

4. Results and discussion

Consistency of regional and global greenness and vegetated areal coverage products generated from different satellite sensors and at different times is very important in the long-term monitoring of variability and change in land cover, and carbon cycle

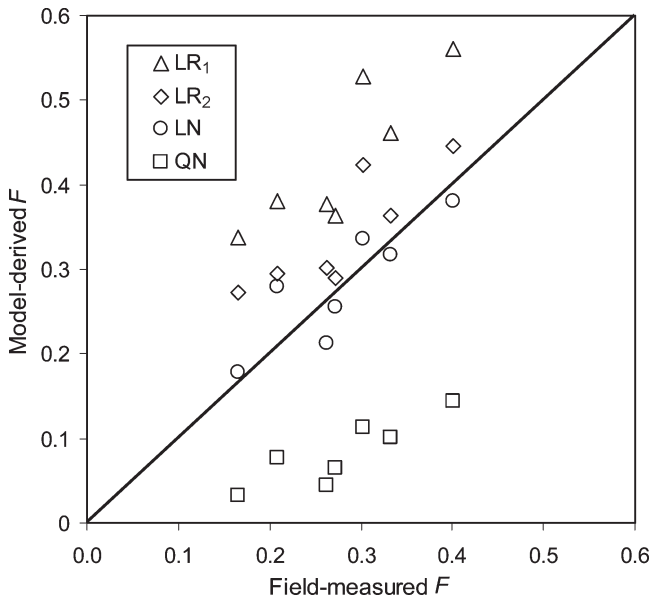


Figure 5. Comparison of model-estimated F and field-measured F within the seven sample cells in the woodland biomass zone. LR₁, linear reflectance model; LR₂, linear reflectance model with shadow correction; LN, linear NDVI model; QN, quadratic NDVI model.

and sequestration by regional and global biospheres. For long-term data analysis and the effective use of remote sensing data from multiple sensors spanning decades, intercomparability and data continuity among these sensor systems are necessary (Vogelmann *et al.* 2001, Thenkabail 2004). NDVIs derived from different sensors are sensor dependent (Steven *et al.* 2003). Factors that affect the NDVI values if calculated from all three definitions for the same type of vegetation photosynthesizing at the same rates include sun–target–sensor geometry, topography, intensity of incident radiation, atmospheric condition, background soil type, spatial resolution, spectral bandwidth, and the shape of the filter transmittance curves of the sensors, A/D convection and instrument calibration. The filter transmittance curves (also called spectral response functions of the sensor) are integrated in the calibration coefficients and are therefore not given separately (in table 1).

The varieties of NDVI definitions add another dimension of inconsistency and system errors. With the increasing number of sensors in coming years, this situation could become even worse. Fortunately, efforts to evaluate and standardize sensor data for long-term intercomparison studies (e.g. Liang 2001, Bricaud *et al.* 2002, Goward *et al.* 2003, Thenkabail 2004, Soudani *et al.* 2006) and standardize the remote sensing terminology (e.g. Schaepman-Strub *et al.* 2006) have been started and are being actively pursued. Standardization of remote sensing concepts such as the NDVI will eventually contribute to data consistency and system-error reduction among publications in the remote sensing literature.

Our results for six multi- and hyperspectral sensors (ALI, ASTER, ETM+, HRVIR, Hyperion, and IKONOS) show that the difference in NDVI defined by spectral reflectance, spectral radiance and the DN value is sensor dependent but is always significant, especially for vegetated regions. Therefore, the three definitions are not consistent. Optimization is necessary for long-term data consistency; the

NDVI should only be calculated by spectral reflectance. To guarantee the long-term NDVI data availability from characteristically different sensors, intersensor comparability and inter-relationships are being sought (Nouvellon *et al.* 2001, Steven *et al.* 2003, Thenkabail 2004). For instance, Nouvellon *et al.* (2001) reported relationships between ecological variables and spectral-derived indices including the NDVI using Landsat TM and ETM+ data. Steven *et al.* (2003) established an intersensor conversion relationship of the vegetation index for a series of satellite sensors. Thenkabail (2004) established intersensor model equations relating IKONOS NDVI with ETM+ NDVI by intercomparison between these two characteristically distinct sensor systems.

For vegetation areal coverage, a simple and accurate mapping model using remote sensing data is desirable. To achieve this, a simple relationship between the vegetation fractional coverage within a pixel and the pixel NDVI is being actively looked for because it can reduce the burden of identifying the endmembers and the reflectance spectrum of all endmembers in each pixel if unmixing analysis is performed to obtain the vegetation fraction in each pixel.

Physically, the linear reflectance model is a first-order approximation to the radiative interaction between solar radiation and endmembers. When the vegetated surface is composed of spectrally separable and radiometrically isolated endmembers, a mixed pixel can be simplified as a linear combination of endmembers (Adams *et al.* 1986). However, some non-linear interaction resulting from multiple scattering inevitably occurs between surface endmembers (i.e. intermembers), for example between vegetation and soil in the intercanopy space (Guan *et al.* 2008). This interaction increases the probability of photons being absorbed and scattered in various directions by the endmembers, reducing the surface spectral reflectance due to single scattering, which is determined by the single scattering albedo (Zhou *et al.* 2003). The expected consequence is that the linear reflectance mode will perform well in areas where vegetation is sparse and the non-linear effect resulting from multiple scattering is small, and will overestimate the vegetation fraction in areas where vegetation is dense and the non-linear effect is not negligible. The results from the comparison of the linear reflectance model with *in situ* measurements (section 3) show that the linear reflectance model works well in the shrub biomass zone. This may indicate that the non-linear effect due to multiple scattering of light between shrub and bare soil is not so important, which is understandable considering that the vegetation height and LAI are low, and the leaves are small and sparse for the shrub biomass. In the piñon-juniper biomass zone, the linear reflectance mode with or without shadow correction overestimates the fractional vegetation coverage. This may indicate that non-linearity cannot be neglected in piñon-juniper woodlands, which is consistent with the above observation in the shrub biomass zone, considering that the piñon-juniper trees are much higher and LAI is much larger than creosote shrubs. For this case, a non-linear spectral mixing analysis should be considered (Roberts *et al.* 1993, Borel and Gerstl 1994, Ray and Murray 1996).

The vegetation shadow decreases the total spectral reflectance by adding a new surface endmember with near-zero spectral reflectance (figure 4). Comparison studies with and without shadow correction indicate that the shadow effect in the shrub biomass zone is negligible due to the lower LAI and lower height of the shrubs, which is consistent with the observation that non-linear effect due to multiple scattering is negligible in the shrub biomass zone. However, shadow effects

are clearly observed in the piñon-juniper biomass zone with taller vegetation and a higher canopy LAI (see table 5 and figure 5). The estimation of F from the linear reflectance model in the piñon-juniper biomass zone improved significantly after shadow correction was performed (figure 5).

Based on the optimized NDVI definition, assessment of the three vegetation fraction models by comparison with *in situ* measurement in section 3 shows that the linear NDVI model underestimates F in the shrub biomass zone, whereas it gives good estimates in the piñon-juniper woodland zone (figure 5 and table 5). Coca *et al.* (2004) reported that the NDVI-based model works well for pine forest but not for grassland; and Riaño *et al.* (2002) reported that NDVI models work well in estimating F for the mixed chaparral in northern California but not for coastal sage scrub. Our comparison study shows that no significant difference was found between the derived vegetation fractions with and without shadow correction from the linear NDVI model in the piñon-juniper biomass zone. This may suggest that the different performance of the linear NDVI model between the shrub biomass zone and the piñon-juniper biomass zone is due to site-specific characteristics such as canopy LAI and vegetation height rather than shadow effects (Gutman and Ignatov 1998). One possible reason for the good performance of the linear NDVI model in the piñon-juniper biomass zone is that the NDVI can partially capture non-linearity in the interaction between radiation and the piñon-juniper woodland. Our results show that the quadratic NDVI model generally underestimates F in both shrub and piñon-juniper biomass zones (figure 5 and table 5). We should point out, however, that the vegetation areal fraction estimated from the NDVI-based models may be more accurately referred to as the areal fraction of greenness because the NDVI is more a measure of greenness, whereas the vegetation areal coverage includes green leaves, senesced leaves, branches, trunks, and litter. However, as our measurement of areal fraction was on perennial vegetation (both creosote shrub and piñon-juniper) and in an actively growing season (June), this difference is neglected.

Comparisons of the linear reflectance model and the NDVI-based models by other researchers (McGwire *et al.* 2000, North 2002, Riaño *et al.* 2002, Coca *et al.* 2004) suggest that the linear reflectance model usually outperforms the linear NDVI model. Some of the studies show that F correlates well with the NDVI in high LAI vegetation (Riaño *et al.* 2002, Coca *et al.* 2004). Our results suggest that the vegetation fraction derived from the linear reflectance model agrees better than the other two models in the shrub biomass zone (low LAI regions) and the linear NDVI model outperforms the other two in the piñon-juniper biomass zone (high LAI regions). In our assessment, the atmospheric effect was appropriately corrected for but the bidirectional correction was not performed. As our assessment was carried out using ETM+ data whose viewing zenith is in nadir and the *in situ* measurements of spectral reflectance were also acquired with optics in nadir, the directional effect is deemed negligible (Levin *et al.* 2004).

5. Conclusions

We conclude that: (1) spectral reflectance should always be used in calculating the NDVI. Using spectral radiance to calculate the NDVI defined by spectral reflectance always underestimates the NDVI and results in an absolute error as high as 0.14 for ALI, 0.15 for IKONOS, 0.16 for ASTER, and 0.20 for ETM+ and HRVIR; the difference in NDVI due to any two of the NDVI definitions is sensor

dependent and is always significant. This is different from the general belief that using the DN value, spectral radiance or spectral reflectance often has little impact in calculating the NDVI within the context of an individual study (Price 1987, Steven *et al.* 2003). Combing the results from Steven *et al.* (2003), that vegetation indices from different satellite sensors cannot be regarded as directly equivalent, we conclude that the NDVI depends not only on the specific sensor but also on the form that is used to calculate the NDVI. Optimization of NDVI definitions is necessary. (2) Using the DN value or spectral radiance to calculate the NDVI should always be avoided. Using the DN to calculate the NDVI defined by spectral reflectance can result in an error as high as 0.23 (overestimate) for ALI, 0.17 (overestimate) for ASTER, 0.47 (underestimate) for ETM+, 0.39 (underestimate) for HRVIR, 0.15 (underestimate) for Hyperion, and 0.02 (underestimate) for IKONOS. IKONOS is the only sensor thus calibrated that the NDVI defined using spectral reflectance can be estimated using the DN value directly without causing differences greater than 0.02. (3) In deriving the fractional vegetation coverage, the linear reflectance model outperforms the NDVI-based models (linear NDVI and quadratic NDVI models) in the shrub biomass zone. (4) Comparison of the model-derived F with *in situ* measurements shows that the linear NDVI model outperforms the other two models in the piñon-juniper biomass zone. The NDVI models are generally less sensitive to vegetation shadow than the linear reflectance model.

Acknowledgements

This work was supported by the Montana Space Grant Consortium, Montana Tech of the University of Montana, NSF Montana EPSCoR grant EPS-0701906, NSF SAHRA grant EAR-9876800, University of Texas at San Antonio. The Sevilleta Long-Term Ecological Research Program (LTER) at the University of New Mexico supported by NSF is acknowledged for providing remote sensing and GIS data resources, and accessibility to the field research sites. We are grateful to the anonymous reviewers for their very helpful comments and suggestions.

References

- ABRAMS, M., HOOK, S. and RAMACHANDRAN, B., 2002, *ASTER Users Handbook, Version 2*. Jet Propulsion Laboratory. Available online at: http://asterweb.jpl.nasa.gov/content/03_data/04_Documents/.
- ADAMS, J.B., SMITH, M.O. and JOHNSON, P.E., 1986, Spectral mixture modeling: a new analysis of rock and soil types at the Viking Lander I site. *Journal of Geophysical Research*, **91**, pp. 8098–8112.
- ASRAR, G., FUCHS, M., KANEMASU, E.T. and HATFIELD, J.L., 1984, Estimating absorbed photosynthetic radiation and leaf area index from spectral reflectance in wheat. *Agronomy Journal*, **76**, pp. 300–306.
- ASNER, G.P. and HEIDEBRECHT, K.B., 2002, Spectral unmixing of vegetation, soil and dry carbon cover in arid regions: comparing multispectral and hyperspectral observations. *International Journal of Remote Sensing*, **23**, pp. 3939–3958.
- ASNER, G.P., NEPSTAD, D., CARDINOT, G. and RAY, D., 2004, Drought stress and carbon uptake in an Amazon forest measured with spaceborne imaging spectroscopy. *Proceedings of the National Academy of Sciences of the United States of America*, **101**, pp. 6039–6044.
- BANNARI, A., MORIN, D. and BONN, F., 1995, A review of vegetation indices. *Remote Sensing Reviews*, **13**, pp. 95–120.
- BOREL, C.C. and GERSTL, S.A.W., 1994, Nonlinear spectra mixing models for vegetative and soil surfaces. *Remote Sensing of Environment*, **47**, pp. 403–416.

- BRICAUD, A., BOSCH, E. and ANTOINE, D., 2002, Algal biomass and sea surface temperature in the Mediterranean basin: intercomparison of data from various satellite sensors, and implications for primary production estimates. *Remote Sensing of Environment*, **81**, pp. 163–178.
- BUSCHMANN, C. and NAGEL, E., 1993, *In vivo* spectroscopy and internal optics of leaves as basis for remote sensing of vegetation. *International Journal of Remote Sensing*, **14**, pp. 711–722.
- CAMPBELL, J.B., 1987, *Introduction to Remote Sensing* (New York: Guilford Press).
- CARLSON, T.N. and RIPLEY, D.A., 1997, On the relation between NDVI, fraction vegetation cover, and leaf area index. *Remote Sensing of Environment*, **62**, pp. 241–252.
- CHAVEZ, P.S., 1996, Image-based atmospheric corrections – revisited and improved. *Photogrammetric Engineering and Remote Sensing*, **62**, pp. 1025–1036.
- CHEN, X., VIERLING, L., ROWELL, E. and DEFELICE, T., 2004, Using lidar and effective LAI data to evaluate IKONOS and Landsat 7 ETM+ vegetation cover estimates in a ponderosa pine forest. *Remote Sensing of Environment*, **91**, pp. 14–26.
- CHOUHDURY, B.J., AHMED, H.U., IDSO, S.B., REGINATO, R.J. and DAUGHTRY, C.S.T., 1994, Relations between evaporation coefficients and vegetation indices studied by model simulations. *Remote Sensing of Environment*, **50**, pp. 1–17.
- CHRYSOULAKIS, N., 2003, Estimation of the all-wave urban surface radiation balance by use of ASTER multispectral imagery and in situ spatial data. *Journal of Geophysical Research*, **108**, pp. D18, 4582, doi:10.1029/2003JD003396.
- CIHLAR, J., ST-LAURENT, L. and DYER, J.A., 1991, Relation between the normalized difference vegetation index and ecological variables. *Remote Sensing of Environment*, **35**, pp. 279–289.
- COCA, F.C., GARCA-HARO, F.J., GILABERT, M.A. and MELIÁ, J., 2004, Vegetation cover seasonal changes assessment from TM imagery in a semi-arid landscape. *International Journal of Remote Sensing*, **25**, pp. 3451–3476.
- COLOMBO, R., BELLINGERI, D., FASOLINI, D. and MARINO, C.M., 2003, Retrieval of leaf area index in different vegetation types using high resolution satellite data. *Remote Sensing of Environment*, **86**, pp. 120–131.
- DAUGHTRY, C.S.T., GALLO, K.P., GOWARD, S.N., PRINCE, S.D. and KUSTAS, W.P., 1992, Spectral estimates of absorbed radiation and phytomass production in corn and soybean canopies. *Remote Sensing of Environment*, **39**, pp. 141–152.
- DIAL, G., BOWEN, H., GERLACH, F., GRODECKI, J. and OLESZCZUK, R., 2003, IKONOS satellite, imagery, and products. *Remote Sensing of Environment*, **88**, pp. 23–36.
- DUFFIE, J.A. and BECKMAN, W.A., 1991, *Solar Engineering of Thermal Processes* (New York: John Wiley and Sons).
- GERTNER, G., WANG, G., FANG, S. and ANDERSON, A.B., 2002, Mapping and uncertainty of predictions based on multiple primary variables from joint co-simulation with Landsat TM image and polynomial regression. *Remote Sensing of Environment*, **83**, pp. 498–510.
- GILLIES, R.R., CARLSON, T.N., CUI, J., KUSTAS, W.P. and HUMES, K.S., 1997, A verification of the ‘triangle’ method for obtaining surface soil water content and energy fluxes from remote measurements of the Normalized Difference Vegetation Index (NDVI) and surface radiant temperature. *International Journal of Remote Sensing*, **18**, pp. 3145–3166.
- GOWARD, S.N., DAVIS, P.E., FLEMING, D., MILLER, L. and TOWNSHEND, J.R., 2003, Empirical comparison of Landsat 7 and IKONOS multispectral measurements for selected Earth Observation System (EOS) validation sites. *Remote Sensing of Environment*, **88**, pp. 80–99.
- GUAN, H., XIE, H. and ZHU, M., 2008, Canopy blockage and scattering effects on apparent soil spectral reflectance and its consequence in spectral mixture analysis of vegetated surfaces. *International Journal of Remote Sensing*, **29**, pp. 3509–3522.

- GUPTA, R.K., VIJAYAN, D. and PRASAD, T.S., 2001, New hyperspectral vegetation characterization parameters. *Advances in Space Research*, **28**, pp. 201–206.
- GUTMAN, G. and IGNATOV, A., 1998, The derivation of the green vegetation fraction from NOAA/AVHRR data for use in numerical weather prediction models. *International Journal of Remote Sensing*, **19**, pp. 1533–1543.
- GUYOT, G. and GU, X.F., 1994, Effect of radiometric corrections on NDVI determined from SPOT HRV and Landsat TM data. *Remote Sensing of Environment*, **49**, pp. 169–180.
- HOBBIE, J.E., CARPENTER, S.R., GRIMM, N.B., GOSZ, J.R. and SEASTEDT, T.R., 2003, The US Long Term Ecological Research Program. *BioScience*, **53**, pp. 21–32.
- HUETE, A.R. and TUCKER, C.J., 1991, Investigation of soil influences in AVHRR red and near-infra-red vegetation index imagery. *International Journal of Remote Sensing*, **12**, pp. 1223–1242.
- HUNT, E.R., Jr., FAHNESTOCK, J.T., KELLY, R.D., WELKER, J.M., REINERS, W.A. and SMITH, W.K., 2002, Carbon sequestration from remotely sensed NDVI and net ecosystem exchange. In *From Laboratory Spectroscopy to Remotely Sensed Spectra of Terrestrial Ecosystems*, R.S. Muttiah (Ed.), pp. 161–174 (Dordrecht, the Netherlands: Kluwer).
- INGRAM, J.C., DAWSON, T.P. and WHITTAKER, R.J., 2005, Mapping tropical forest structure in southeastern Madagascar using remote sensing and artificial neural networks. *Remote Sensing of Environment*, **94**, pp. 491–507.
- JOHNSON, L.F., ROCZEN, D.E., YOUKHANA, S.K., NEMANI, R.R. and BOSCH, D.F., 2003, Mapping vineyard leaf area with multispectral satellite imagery. *Computers and Electronics in Agriculture*, **38**, pp. 33–44.
- JUSTICE, C.O., TOWNSHEND, J.G.R., HOLBEN, B.N. and TUCKER, C.J., 1985, Analysis of the phenology of global vegetation using meteorological satellite data. *International Journal of Remote Sensing*, **6**, pp. 1271–1318.
- KALÁCSKA, M., SÁNCHEZ-AZOFEIFA, G.A., RIVARD, B., CALVO-ALVARADO, J.C., JOURNET, A.R.P., ARROYO-MORA, J.P. and ORTIZ-ORTIZ, D., 2004, Leaf area index measurements in a tropical moist forest: a case study from Costa Rica. *Remote Sensing of Environment*, **91**, pp. 134–152.
- KARNIELI, A., GABAI, A., ICHOKU, C., ZAADY, E. and SHACHAK, M., 2002, Temporal dynamics of soil and vegetation spectral responses in a semi-arid environment. *International Journal of Remote Sensing*, **23**, pp. 4073–4087.
- KURC, S.A. and SMALL, E.E., 2004, Dynamics of evapotranspiration in semiarid grassland and shrubland during the summer monsoon season, central New Mexico. *Water Resources Research*, **40**, W09305, doi:10.1029/2004WR003068.
- LEPRIEUR, C., KERR, Y.H., MASTORCHIO, S. and MEUNIER, J.C., 2000, Monitoring vegetation cover across semi-arid regions: comparison of remote sensing observation from various scales. *International Journal of Remote Sensing*, **21**, pp. 281–300.
- LEVIN, N., BEN-DOR, E. and KARNIELI, A., 2004, Topographic information of sand dunes as extracted from shading effects using Landsat images. *Remote Sensing of Environment*, **90**, pp. 190–209.
- LIANG, S., 2001, Narrowband to broadband conversions of land surface albedo: I. Algorithms. *Remote Sensing of Environment*, **76**, pp. 213–238.
- LU, H., RAUPACH, M.R., McVICAR, T.R. and BARRETT, D.J., 2003, Decomposition of vegetation cover into woody and herbaceous components using AVHRR NDVI time series. *Remote Sensing of Environment*, **86**, pp. 1–18.
- MCGWIRE, K., MINOR, T. and FENSTERMAKER, L., 2000, Hyperspectral mixture modeling for quantifying sparse vegetation cover in arid environments. *Remote Sensing of Environment*, **72**, pp. 360–374.
- MORAN, M.S., JACKSON, R.D., SLATER, P.N. and TEILLET, P.M., 1992, Evaluation of simplified procedures for retrieval of land surface reflectance factors from satellite sensor output. *Remote Sensing Environment*, **41**, pp. 169–184.

- MORISSETTE, J.T., NICKESON, J.E., DAVIS, P., WANG, Y., TIAN, Y., WOODCOCK, C.E., SHABANOV, N., HANSEN, M., COHEN, W.B., OETTER, D.R. and KENNEDY, R.E., 2003, High spatial resolution satellite observations for validation of MODIS land products: IKONOS observations acquired under the NASA Scientific Data Purchase. *Remote Sensing of Environment*, **88**, pp. 100–110.
- MYNENI, R.B., HALL, F.G., SELLERS, P.J. and MARSHAK, A.L., 1995, The interpretation of spectral vegetation indices. *IEEE Transactions on Geoscience and Remote Sensing*, **33**, pp. 481–486.
- NASA, 2002, *Earth Observing-1: Advanced Land Imager* (Greenbelt, MD: National Aeronautics and Space Administration/Goddard Space Flight Center). Available online at: <http://eo1.gsfc.nasa.gov/Technology/ALHome1.htm>.
- NASA, 2006, *Landsat-7 Science Data User's Handbook* (Greenbelt, MD: National Aeronautics and Space Administration/Goddard Space Flight Center). Available online at: <http://landsathandbook.gsfc.nasa.gov/handbook.html>.
- NEMANI, R., PIERCE, L., RUNNING, S.W. and BAND, L., 1993, Forest ecosystem processes at the watershed scale: sensitivity to remotely sensed leaf area index estimates. *International Journal of Remote Sensing*, **14**, pp. 2519–2534.
- NORTH, P.R.J., 2002, Estimation of fAPAR, LAI, and vegetation fractional cover from ATSR-2 imagery. *Remote Sensing of Environment*, **80**, pp. 114–121.
- NOUVELLON, Y., MORAN, M.S., SEEN, D.L., BRYANT, R., RAMBAL, S., NI, W., BÉGUÉ, A., CHEHBOUNI, A., EMMERICHA, W.E., HEILMAN, P. and QI, J., 2001, Coupling a grassland ecosystem model with Landsat imagery for a 10-year simulation of carbon and water budgets. *Remote Sensing of Environment*, **78**, pp. 131–149.
- OKIN, G.S., ROBERTS, D.A., MURRAY, B. and OKIN, W.J., 2001, Practical limits on hyperspectral vegetation discrimination in arid and semiarid environments. *Remote Sensing of Environment*, **77**, pp. 212–225.
- OGURO, Y., SUGA, Y., TAKEUCHI, S., OGAWA, M., KONISHI, T. and TSUCHIYA, K., 2001, Comparison of SAR and optical sensor data for monitoring of rice plant around Hiroshima. *Advances in Space Research*, **28**, pp. 195–200.
- PARUELO, J.M. and LAUENROTH, W.K., 1995, Regional patterns of normalized difference vegetation index in North American shrublands and grasslands. *Ecology*, **76**, pp. 1888–1898.
- PEARLMAN, J.S., 2003, *Hyperion Validation Report*. Boeing Report Number 03-ANCOS-001, 16 July 2003. Available online at: <http://eo1.gsfc.nasa.gov/new/validationReport/Technology/Documents/Reports/Hyperion.pdf>.
- PETERSON, D.L., PRICE, K.P. and MARTINKO, E.A., 2002, Discriminating between cool season and warm season grassland cover types in northeastern Kansas. *International Journal of Remote Sensing*, **23**, pp. 5015–5030.
- PRICE, J.C., 1987, Calibration of satellite radiometers and the comparison of vegetation indices. *Remote Sensing of Environment*, **21**, pp. 15–27.
- QI, J., MARSETT, R.C., MORAN, M.S., GOODRICH, D.C., HEILMAN, P., KERR, Y.H., DEDIEU, G., CHEHBOUNI, A. and ZHANG, X.X., 2000, Spatial and temporal dynamics of vegetation in the San Pedro River basin area. *Agricultural and Forest Meteorology*, **105**, pp. 55–68.
- RAY, T.W. and MURRAY, B.C., 1996, Nonlinear spectral mixing in desert vegetation. *Remote Sensing of Environment*, **55**, pp. 59–64.
- RIAÑO, D., CHUVIECO, E., USTIN, S., ZOMER, R., DENNISON, P., ROBERTS, D. and SALAS, J., 2002, Assessment of vegetation regeneration after fire through multitemporal analysis of AVIRIS images in the Santa Monica Mountains. *Remote Sensing of Environment*, **79**, pp. 60–71.
- ROBERTS, D.A., SMITH, M.O. and ADAMS, J.B., 1993, Green vegetation, nonphotosynthetic vegetation, and soils in AVIRIS data. *Remote Sensing of Environment*, **44**, pp. 255–269.

- ROBERTS, D.A., GARDNER, M., CHURCH, R., USTIN, S., SCHEER, G. and GREEN, R.O., 1998, Mapping chaparral in the Santa Monica Mountains using multiple endmember spectral mixture models. *Remote Sensing of Environment*, **65**, pp. 267–279.
- RODERICK, M., SMITH, R. and CRIDLAND, S., 1996, The precision of the NDVI derived from AVHRR observations. *Remote Sensing of Environment*, **56**, pp. 57–65.
- ROUSE, J.W., 1973, *Monitoring the Vernal Advancement and Retrogradation of Natural Vegetation. NASA/GSFCT Type II Report (Greenbelt, MD: NASA)*.
- RUIZ, J.A.M. and GARBN, M.C., 2004, Estimating burned area for tropical Africa for the year 1990 with the NOAA-NASA Pathfinder AVHRR 8km land dataset. *International Journal of Remote Sensing*, **25**, pp. 3389–3410.
- RUNNING, S.W., BALDOCCHI, D.D., TURNER, D.P., GOWER, S.T., BAKWIN, P.S. and HIBBARD, K.A., 1999, A global terrestrial monitoring network integrating tower fluxes, flask sampling, ecosystem modeling and EOS satellite data. *Remote Sensing of Environment*, **70**, pp. 108–127.
- SCHAEPMAN-STRUB, G., SCHAEPMAN, M.E., PAINTER, T.H., DANGEL, S. and MARTONCHIK, J.V., 2006, Reflectance quantities in optical remote sensing – definitions and case studies. *Remote Sensing of Environment*, **103**, pp. 27–42.
- SCHROEDER, M., POUTIER, L., MÜLLER, R., DINGUIRARD, M., REINARTZ, P. and BRIOTTET, X., 2001, Intercalibration of optical satellites – a case study with MOMS and SPOT. *Aerospace Science and Technology*, **5**, pp. 305–315.
- SHABANOV, N.V., HUANG, D., YANG, W., TAN, B., KNYAZIKHIN, Y., MYNENI, R.B., AHL, D.E., GOWER, S.T. and HUETE, A.R., 2005, Analysis and optimization of the MODIS leaf area index algorithm retrievals over broadleaf forests. *IEEE Transactions on Geoscience and Remote Sensing*, **75**, pp. 230–244.
- SMITH, M.O., USTIN, S.L., ADAMS, J.B. and GILLESPIE, A.R., 1990a, Vegetation in deserts, I. A regional measure of abundance from multispectral images. *Remote Sensing of Environment*, **31**, pp. 1–26.
- SMITH, M.O., USTIN, S.L., ADAMS, J.B. and GILLESPIE, A.R., 1990b, Vegetation in deserts, II. Environmental influences on regional abundance. *Remote Sensing of Environment*, **31**, pp. 27–52.
- SONG, C., WOODCOCK, C.E., SETO, K.C., LENNEY, M.P. and MACOMBER, S.A., 2001, Classification and change detection using Landsat TM data: when and how to correct atmospheric effects? *Remote Sensing of Environment*, **75**, pp. 230–244.
- SOUDANI, K., FRANÇOIS, C., LE MAIRE, G., LE DANTEC, V. and DUFRÊNE, E., 2006, Comparative analysis of IKONOS, SPOT, and ETM+ data for leaf area index estimation in temperate coniferous and deciduous forest stands. *Remote Sensing of Environment*, **102**, pp. 161–175.
- STEVEN, M.D., MALTHUS, T.J., BARET, F., XU, H. and CHOPPING, M.J., 2003, Intercalibration of vegetation indices from different sensor systems. *Remote Sensing of Environment*, **88**, pp. 412–422.
- THENKABAIL, P.S., 2004, Inter-sensor relationships between IKONOS and Landsat-7 ETM+ NDVI data in three ecoregions of Africa. *International Journal of Remote Sensing*, **25**, pp. 389–408.
- THENKABAIL, P.S., ENCLONA, E.A., ASHTON, M.S., LEGG, C. and DE DIEU, M.J., 2004, Hyperion, IKONOS, ALI, and ETM+ sensors in the study of African rainforests. *Remote Sensing of Environment*, **90**, pp. 23–43.
- TUCKER, C.J., 1979, Red and photographic infrared linear combinations for monitoring vegetation. *Remote Sensing of Environment*, **8**, pp. 127–150.
- TUCKER, C.J., TOWNSHEND, J.R.G. and GOFF, T.E., 1985a, African land-cover classification using satellite data. *Science*, **227**, pp. 369–375.
- TUCKER, C.J., VANPRAET, C.L., SHARMAN, M.J. and VAN ITTERSUM, G., 1985b, Satellite remote sensing of total herbaceous biomass production in the Senegalese Sahel: 1980–1984. *Remote Sensing of Environment*, **17**, pp. 233–249.

- TURNER, D.P., COHEN, W.B., KENNEDY, R.E., FASSNACHT, K.S. and BRIGGS, J.M., 1999, Relationships between leaf area index and Landsat TM spectral vegetation indices across three temperate zone sites. *Remote Sensing of Environment*, **70**, pp. 52–68.
- ÜNSALAN, C. and BOYER, K.L., 2004, Linearized vegetation indices based on a formal statistical framework. *IEEE Transactions on Geoscience and Remote Sensing*, **42**, pp. 1575–1585.
- USGS, 2006, *EO-1 User's Guide* (Sioux Falls, SD: United States Geological Survey EROS Data Center). Available online at: <http://eo1.usgs.gov/userGuide/>.
- VIERLING, L.A., DEERING, D.W. and ECK, T.F., 1997, Differences in arctic tundra vegetation type and phenology as seen using bidirectional radiometry in the early growing season. *Remote Sensing of Environment*, **60**, pp. 71–82.
- VOGELMANN, J.E., HELDER, D., MORFITT, R., CHOATE, M.J., MERCHANT, J.W. and BULLEY, H., 2001, Effects of Landsat 5 Thematic Mapper and Landsat 7 Enhanced Thematic Mapper Plus radiometric and geometric calibrations and corrections on landscape characterization. *Remote Sensing of Environment*, **78**, pp. 55–70.
- WITTICH, K.P. and HANSING, O., 1995, Area-averaged vegetative cover fraction estimated from satellite data. *International Journal of Biometeorology*, **38**, pp. 209–215.
- XIE, H., TIAN, Y.Q., GRANILLO, J.A. and KELLER, G.R., 2007, Suitable remote sensing method and data for mapping and measuring active crop field. *International Journal of Remote Sensing*, **28**, pp. 395–411.
- ZENG, X.B., DICKINSON, R.E., WALKER, A., SHAIKH, M., DEFRIES, R.S. and QI, J.G., 2000, Derivation and evaluation of global 1-km fractional vegetation cover data for land modeling. *Journal of Applied Meteorology*, **39**, pp. 826–839.
- ZHOU, X., LI, S. and STAMNES, K., 2003, Geometrical-optics code for computing the optical properties of large dielectric spheres. *Applied Optics*, **42**, pp. 4295–4306.